

RANDOM WEIGHT FACTORIZATION IMPROVES THE TRAINING OF CONTINUOUS NEURAL REPRESENTATIONS

Sifan Wang, Hanwen Wang, Jacob H. Seidman, Paris Perdikaris

University of Pennsylvania, Philadelphia, PA 19104

{sifanw, wangh19, seidj@sas.upenn.edu}@sas.upenn.edu,
pgp@seas.upenn.edu

ABSTRACT

Continuous neural representations have recently emerged as a powerful and flexible alternative to classical discretized representations of signals. However, training them to capture fine details in multi-scale signals is difficult and computationally expensive. Here we propose *random weight factorization* as a simple drop-in replacement for parameterizing and initializing conventional linear layers in coordinate-based multi-layer perceptrons (MLPs) that significantly accelerates and improves their training. We show how this factorization alters the underlying loss landscape and effectively enables each neuron in the network to learn using its own self-adaptive learning rate. This not only helps with mitigating spectral bias, but also allows networks to quickly recover from poor initializations and reach better local minima. We demonstrate how *random weight factorization* can be leveraged to improve the training of neural representations on a variety of tasks, including image regression, shape representation, computed tomography, inverse rendering, solving partial differential equations, and learning operators between function spaces.

1 INTRODUCTION

Some of the recent advances in machine learning can be attributed to new developments in the design of *continuous neural representations*, which employ coordinate-based multi-layer perceptrons (MLPs) to parameterize discrete signals (e.g. images, videos, point clouds) across space and time. Such parameterizations are appealing because they are differentiable and much more memory efficient than grid-sampled representations, naturally allowing smooth interpolations to unseen input coordinates. As such, they have achieved widespread success in a variety of computer vision and graphics tasks, including image representation (Stanley, 2007; Nguyen et al., 2015), shape representation (Chen & Zhang, 2019; Park et al., 2019; Genova et al., 2019; 2020), view synthesis (Sitzmann et al., 2019; Saito et al., 2019; Mildenhall et al., 2020; Niemeyer et al., 2020), texture generation (Oechsle et al., 2019; Henzler et al., 2020), etc. Coordinate-based MLPs have also been applied to scientific computing applications such as physics-informed neural networks (PINNs) for solving forward and inverse partial differential equations (PDEs) Raissi et al. (2019; 2020); Karniadakis et al. (2021), and Deep Operator networks (DeepONets) for learning operators between infinite-dimensional function spaces Lu et al. (2021); Wang et al. (2021e).

Despite their flexibility, it has been shown both empirically and theoretically that coordinate-based MLPs suffer from “spectral bias” (Rahaman et al., 2019; Cao et al., 2019; Xu et al., 2019). This manifests as a difficulty in learning the high frequency components and fine details of a target function. A popular method to resolve this issue is to embed input coordinates into a higher dimensional space, for example by using Fourier features before the MLP (Mildenhall et al., 2020; Tancik et al., 2020). Another widely used approach is the use of SIREN networks (Sitzmann et al., 2020), which employs MLPs with periodic activations to represent complex natural signals and their derivatives. One main limitation of these methods is that a number of associated hyper-parameters (e.g. scale factors) need to be carefully tuned in order to avoid catastrophic generalization/interpolation errors.

Unfortunately, the selection of appropriate hyper-parameters typically requires some prior knowledge about the target signals, which may not be available in some applications.

More general approaches to improve the training and performance of MLPs involve different types of normalizations, such as Batch Normalization (Ioffe & Szegedy, 2015), Layer Normalization (Ba et al., 2016) and Weight Normalization (Salimans & Kingma, 2016). However, despite their remarkable success in deep learning benchmarks, these techniques are not widely used in MLP-based neural representations. Here we draw motivation from the work of (Salimans & Kingma, 2016; Wang et al., 2021a) and investigate a simple yet remarkably effective re-parameterization of weight vectors in MLP networks, coined as *random weight factorization*, which provides a generalization of Weight Normalization and demonstrates significant performance gains. Our main contributions are summarized as

- We show that *random weight factorization* alters the loss landscape of a neural representation in a way that can drastically reduce the distance between different parameter configurations, and effectively assigns a self-adaptive learning rate to each neuron in the network.
- We empirically illustrate that *random weight factorization* can effectively mitigate spectral bias, as well as enable coordinate-based MLP networks to escape from poor initializations and find better local minima.
- We demonstrate that *random weight factorization* can be used as a simple drop-in enhancement to conventional linear layers, and yield consistent and robust improvements across a wide range of tasks in computer vision, graphics and scientific computing.

2 WEIGHT FACTORIZATION

Let $\mathbf{x} \in \mathbb{R}^d$ be the input, $\mathbf{g}^{(0)}(\mathbf{x}) = \mathbf{x}$ and $d_0 = d$. We consider a standard multi-layer perceptron (MLP) $f_{\theta}(\mathbf{x})$ recursively defined by

$$\mathbf{f}_{\theta}^{(l)}(\mathbf{x}) = \mathbf{W}^{(l)} \cdot \mathbf{g}^{(l-1)}(\mathbf{x}) + \mathbf{b}^{(l)}, \quad \mathbf{g}^{(l)}(\mathbf{x}) = \sigma(\mathbf{f}_{\theta}^{(l)}(\mathbf{x})), \quad l = 1, 2, \dots, L, \quad (2.1)$$

with a final layer

$$f_{\theta}(\mathbf{x}) = \mathbf{W}^{(L+1)} \cdot \mathbf{g}^{(L)}(\mathbf{x}) + \mathbf{b}^{(L+1)}, \quad (2.2)$$

where $\mathbf{W}^{(l)} \in \mathbb{R}^{d_l \times d_{l-1}}$ is the weight matrix in l -th layer and σ is an element-wise activation function. Here, $\theta = (\mathbf{W}^{(1)}, \mathbf{b}^{(1)}, \dots, \mathbf{W}^{(L+1)}, \mathbf{b}^{(L+1)})$ represents all trainable parameters in the network.

MLPs are commonly trained by minimizing an appropriate loss function $\mathcal{L}(\theta)$ via gradient descent. To improve convergence, we propose to factorize the weight parameters associated with each neuron in the network as follows

$$\mathbf{w}^{(k,l)} = s^{(k,l)} \cdot \mathbf{v}^{(k,l)}, \quad k = 1, 2, \dots, d_l, \quad l = 1, 2, \dots, L+1, \quad (2.3)$$

where $\mathbf{w}^{(k,l)} \in \mathbb{R}^{d_{l-1}}$ is a weight vector representing the k -th row of the weight matrix $\mathbf{W}^{(l)}$, $s^{(k,l)} \in \mathbb{R}$ is a trainable scale factor assigned to each individual neuron, and $\mathbf{v}^{(k,l)} \in \mathbb{R}^{d_{l-1}}$. Consequently, the proposed weight factorization can be written by

$$\mathbf{W}^{(l)} = \text{diag}(\mathbf{s}^{(l)}) \cdot \mathbf{V}^{(l)}, \quad l = 1, 2, \dots, L+1. \quad (2.4)$$

with $\mathbf{s} \in \mathbb{R}^{d_l}$.

2.1 A GEOMETRIC PERSPECTIVE

In this section, we provide a geometric motivation for the proposed weight factorization. To this end, we consider the simplest setting of a one-parameter loss function $\ell(w)$. For this case, the weight factorization is reduced to $w = s \cdot v$ with two scalars s, v . Note that for a given $w \neq 0$ there are infinitely many pairs (s, v) such that $w = s \cdot v$. The set of such pairs forms a family of hyperbolas in the sv -plane (one for each choice of signs for both s and v). As such, the loss function in the sv -plane is constant along these hyperbolas.

Figure 1 gives a visual illustration of the difference between the original loss landscape as a function of w versus the loss landscape in the factorized sv -plane. In the left panel, we plot the original loss function as well as an initial parameter point, the local minimum, and the global minimum. The right panel shows how in the factorized parameter

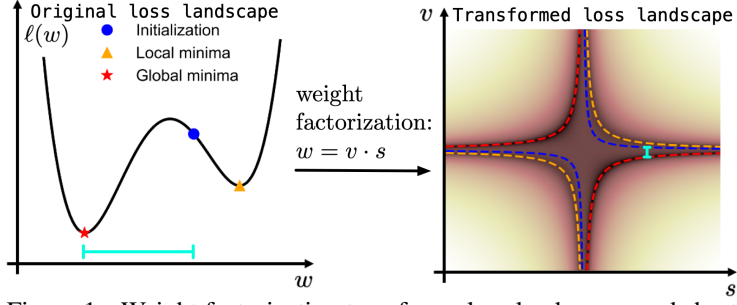


Figure 1: Weight factorization transforms loss landscapes and shortens the distance to minima.

space, each of these three points corresponds to two hyperbolas in the sv -plane. Note how the distance between the initialization and the global minima is reduced from the top to the bottom panel upon an appropriate choice of factorization. The key observation is that the distance between factorizations representing the initial parameter and the global minimum become arbitrarily small in the sv -plane for larger values of s . Indeed, we can prove that this holds for any general loss function in arbitrary parameter dimensions (the proof is provided in Appendix A.1).

Theorem 1. Suppose that $\mathcal{L}(\theta)$ is the associated loss function of a neural network defined in equation 2.1 and equation 2.2. For a given θ , we define U_θ as the set containing all possible weight factorizations

$$U_\theta = \left\{ (s^{(l)}, V^{(l)})_{l=1}^{L+1} : \text{diag}(s^{(l)}) \cdot V^{(l)} = W^{(l)}, \quad l = 1, \dots, L+1 \right\}. \quad (2.5)$$

Then for any θ, θ' , we have

$$\text{dist}(U_\theta, U_{\theta'}) = 0. \quad (2.6)$$

2.2 SELF-ADAPTIVE LEARNING RATE FOR EACH NEURON

A different way to examine the effect of the proposed weight factorization is by studying its associated gradient updates. Recall that a standard gradient descent update with a learning rate η takes the form

$$w_{n+1}^{(k,l)} = w_n^{(k,l)} - \eta \frac{\partial \mathcal{L}}{\partial w_n^{(k,l)}}. \quad (2.7)$$

The following theorem derives the corresponding gradient descent update expressed in the original parameter space for models using the proposed weight factorization.

Theorem 2. Under the weight factorization of equation 2.3, the gradient descent update is given by

$$w_{n+1}^{(k,l)} = w_n^{(k,l)} - \eta \left(\| [s_n^{(k,l)}]^2 + v_n^{(k,l)} \|^2 \right) \frac{\partial \mathcal{L}}{\partial w_n^{(k,l)}} + \mathcal{O}(\eta^2), \quad (2.8)$$

for $l = 1, 2, \dots, L+1$ and $k = 1, 2, \dots, d_l$.

The proof is provided in Appendix A.2. By comparing equation 2.7 and equation 2.8, we observe that the weight factorization $w = s \cdot v$ re-scales the learning rate of w by a factor of $(s^2 + \|v\|_2^2)$. Since s, v are trainable parameters, this analysis suggests that this weight factorization effectively assigns a self-adaptive learning rate to each neuron in the network. In the following sections, we will demonstrate that the proposed weight factorization (under an appropriate initialization of the scale factors), not only helps with mitigating spectral bias (Rahaman et al., 2019; Bietti & Mairal, 2019; Tancik et al., 2020; Wang et al., 2021c), but also allows networks to quickly move away from a poor initialization and reach better local minima faster.

2.3 RELATION TO EXISTING WORKS

The proposed weight factorization is largely motivated by *weight normalization* (Salimans & Kingma, 2016), which decouples the norm and the directions of the weights associated with each

neuron as

$$\mathbf{w} = g \frac{\mathbf{v}}{\|\mathbf{v}\|}, \quad (2.9)$$

where $g = \|\mathbf{w}\|$, and gradient descent updates are applied directly to the new parameters \mathbf{v}, g . Indeed, this can be viewed as a special case of the proposed weight factorization by setting $\mathbf{s} = \|\mathbf{w}\|$ in equation 2.3. In contrast to weight normalization, our weight factorization scheme allows for more flexibility in the choice of the scale factors \mathbf{s} .

We note that SIREN networks (Sitzmann et al., 2020) also employ a special weight factorization for each hidden layer weight matrix,

$$\mathbf{W} = \omega_0 * \hat{\mathbf{W}}, \quad (2.10)$$

where the scale factor $\omega_0 \in \mathbb{R}$ is a user-defined hyper-parameter. Although the authors attribute the success of SIREN to the periodic activation functions in conjunction with a tailored initialization scheme, here we will demonstrate that the specific choice of ω_0 is the most crucial element in SIREN’s performance, see Appendix G, H for more details.

It is worth pointing out that the proposed weight factorization also bears some resemblance to the adaptive activation functions introduced in (Jagtap et al., 2020), which modifies the activation of each neuron by introducing an additional trainable parameter \mathbf{a} as

$$\mathbf{g}^{(l)}(\mathbf{x}) = \sigma(\mathbf{a}\mathbf{f}^{(l)}(\mathbf{x})). \quad (2.11)$$

These adaptive activations aim to help networks learn sharp gradients and transitions of the target functions. In practice, the scale factor is generally initialized as $\mathbf{a} = \mathbf{1}$, yielding a trivial weight factorization. As illustrated in the next section, this is fundamentally different from our approach as we initialize the scale factors \mathbf{s} by a random distribution and re-parameterize the weight matrix accordingly. In Section 4 we demonstrate that, by initializing \mathbf{s} using an appropriate distribution, we can consistently outperform both weight normalization, SIREN, and adaptive activations across a broad range of supervised and self-supervised learning tasks.

3 RANDOM WEIGHT FACTORIZATION IN PRACTICE

Here we illustrate the use of weight factorization through the lens of a simple regression task. Specifically, we consider a smooth scalar-valued function f sampled from a Gaussian random field using a square exponential kernel with a length scale of $l = 0.02$. This generates a data-set of $N = 256$ observation pairs $\{x_i, f(x_i)\}_{i=1}^N$, where $\{x_i\}_{i=1}^N$ lie on a uniform grid in $[0, 1]$. The goal is to train a network f_θ to learn f by minimizing the mean square error loss $\mathcal{L}(\theta) = 1/N \sum_{i=1}^N |f_\theta(x_i) - f(x_i)|^2$.

The proposed random weight factorization is applied as follows. We first initialize the parameters of an MLP network via the Glorot scheme (Glorot & Bengio, 2010). Then, for every weight matrix \mathbf{W} , we proceed by initializing a scale vector $\exp(\mathbf{s})$ where \mathbf{s} is sampled from a multivariate normal distribution $\mathcal{N}(\boldsymbol{\mu}, \sigma\mathbf{I})$. Finally, every weight matrix is factorized by the associated scale factor as $\mathbf{W} = \text{diag}(\exp(\mathbf{s})) \cdot \mathbf{V}$ at initialization. We train this network by gradient descent on the new parameters \mathbf{s}, \mathbf{V} directly. This procedure is summarized in Appendix B, along with a simple JAX Flax implementation (Heek et al., 2020) in Appendix C.

In Figure 2, we train networks (3 layers, 128 neurons per layer, ReLU activations) to learn the target function using: (a) a conventional MLP, (b) an MLP with adaptive activations (AA) (Jagtap et al., 2020), (c) an MLP with weight normalization (WN) (Salimans & Kingma, 2016), and (d) an MLP with the proposed random weight factorization scheme (RWF). Evidently, RWF yields the best predictive accuracy and loss convergence. Moreover, we plot the relative change of the weights in the original (unfactorized) parameter space during training in the bottom middle panel. We observe that RWF leads to the largest weight change during training, thereby enabling the network to find better local minima further away from its initialization. To further emphasize the benefit of weight factorization, we compute the eigenvalues of the resulting empirical Neural Tangent Kernel (NTK) (Jacot et al., 2018)

$$\mathbf{K}_\theta = \left\langle \frac{\partial f_\theta}{\partial \theta}(x_i), \frac{\partial f_\theta}{\partial \theta}(x_j) \right\rangle_{ij}, \quad (3.1)$$

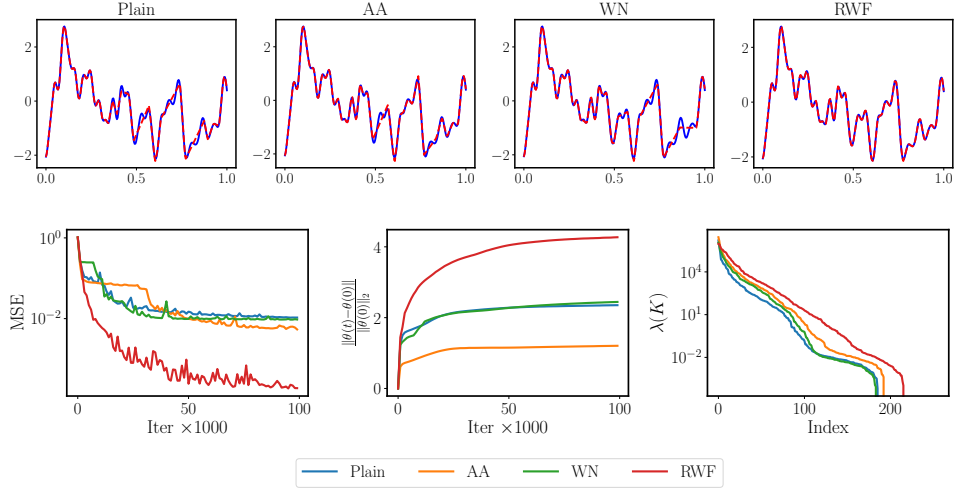


Figure 2: *1D regression*: *Top*: Model predictions using different parameterizations. Plain: Standard MLP; AA: adaptive activation; WN: weight normalization; RWF: random weight factorization. *Bottom left*: Mean square error (MSE) during training. *Bottom Middle*: Relative change of weights during training. The comparison is performed in the original parameter space. *Bottom right*: Eigenvalues (descending order) of the empirical NTK at the end of training.

at the last step of training and visualize them in the bottom right panel. Notice how RWF exhibits a flatter NTK spectrum and slower eigenvalue decay than the other methods, indicating better-conditioned training dynamics and less severe spectral bias, see (Rahaman et al., 2019; Bietti & Mairal, 2019; Tancik et al., 2020; Wang et al., 2021c) for more details. To explore the robustness of the proposed RWF, we conduct a systematic study on the effect of μ and σ in the initialization of the scale factor s . The results suggest that the choice of μ, σ plays an important role. Specifically, too small μ, σ values may lead to performance that is similar to a conventional MLP, while setting μ, σ too large can result in an unstable training process. We empirically find that $\mu = 1, \sigma = 0.1$ consistently improves the loss convergence and model accuracy for the vast majority of tasks considered in this work. Additional details are presented in Appendix D.

4 EXPERIMENTS

In this section, we demonstrate the effectiveness and robustness of *random weight factorization* for training continuous neural representations across a range of tasks in computer vision, graphics, and scientific computing. More precisely, we compare the performance of plain MLPs, MLPs with adaptive activations (AA) (Jagtap et al., 2020), weight normalization (WN) (Salimans & Kingma, 2016), and the proposed random weight factorization (RWF). The comparison is performed over a collection of MLP architectures, including conventional MLPs, SIREN (Sitzmann et al., 2020), modified MLPs (Wang et al., 2021b), as well as MLPs with positional encodings (Mildenhall et al., 2020) and Gaussian Fourier features (Tancik et al., 2020). The hyper-parameters of our experiments along with the computational cost associated with each experiment are presented in Appendix E and Appendix F, respectively. Notice that the computational overhead of our method is marginal, and RWF can be therefore considered as a drop-in enhancement to any architecture that uses linear layers. Table 1 summarizes the results obtained for each benchmark, corresponding to the optimal input mapping and network architecture. Overall, RWF consistently achieves the best performance across tasks and architectures. All code and data will be made publicly available. A summary of each benchmark study is presented below, with more details provided in Appendix.

4.1 2D IMAGE REGRESSION

We train coordinate-based MLPs to learn a map from 2D input pixel coordinates to the corresponding RGB values of an image, using the benchmarks put forth in (Tancik et al., 2020). We conduct experiments using two data-sets: *Natural* and *Text*, each containing 16 images. The *Natural* data-

Task	Metric	Case	Plain	AA	WN	RWF (ours)
Image Regression	PSNR (\uparrow)	Natural	27.35	27.37	27.36	28.08
		Text	32.09	32.29	32.25	33.13
Shape Representation	IoU (\uparrow)	Dragon	0.980	0.981	0.981	0.984
		Armadillo	0.978	0.976	0.974	0.982
Computed Tomography	PSNR (\uparrow)	Shepp	30.09	30.37	30.59	33.73
		ATLAS	21.85	21.93	22.16	23.71
Inverse Rendering	PSNR (\uparrow)	Lego	25.99	25.93	25.93	26.13
Solving PDEs	Rel. L^2 (\downarrow)	Advection	28.82%	38.63%	46.34%	4.14%
		Navier-Stokes	39.25%	34.09%	30.98%	6.67%
Learning Operators	Rel. L^2 (\downarrow)	DR	1.09%	0.95%	0.97%	0.50%
		Darcy	2.03%	2.06%	2.00%	1.67%
		Burgers	5.11%	4.71%	4.37%	2.46%

Table 1: We compare four different parameterizations over various benchmarks, and demonstrate that *Random weight factorization* consistently outperforms other parameterizations across all tasks. All comparisons are conducted under exactly the same hyper-parameter settings. (\uparrow)/(\downarrow) indicates that higher/lower values are better, respectively. (Plain: conventional MLP; AA: adaptive activation; WN: weight normalization; RWF: random weight factorization).

set is constructed by taking center crops of randomly sampled images from the Div2K data-set (Agustsson & Timofte, 2017). The *Text* data-set is constructed by placing random text with random font sizes and colors on a white background. The training data is obtained by downsampling each test image by a factor of 2. We compare the resulting peak signal-to-noise ratio (PSNR) in the full resolution test images, obtained with different MLP architectures using different input mappings and weight parametrizations.

4.2 3D SHAPE REPRESENTATION

This task follows the original problem setup in (Tancik et al., 2020). The goal is to learn an implicit representation of a 3D shape using Occupancy networks (Mescheder et al., 2019), which take spatial coordinates as inputs and predict 0 for points outside a given shape and 1 for points inside the shape. We use two complex triangle meshes commonly used in computer graphics: *Dragon* and *Armadillo*. The training data is generated by randomly sampling points inside a bounding box and calculating their labels using the ground truth mesh. We evaluate the trained model performance using the Intersection over Union (IoU) metric on a set of points randomly sampled near the mesh surface to better highlight the different mappings’ abilities to resolve fine details.

4.3 2D COMPUTED TOMOGRAPHY (CT)

This task follows the original problem setup in (Tancik et al., 2020). We train an MLP to learn a map from 2D pixel coordinates to a corresponding volume density at those locations. Two data-sets are considered: procedurally-generated Shepp-Logan phantoms (Shepp & Logan, 1974) and 2D brain images from the ATLAS data-set (Liew et al., 2018). Different from the previous tasks, we observe integral projections of a density field instead of direct measurements. The network is trained in an indirect supervised fashion by minimizing a loss between a sparse set of ground-truth integral projections and integral projections computed from the network’s output. We use PSNR to quantify the performance of the trained MLPs with different input mappings and different weight parametrizations.

4.4 3D INVERSE RENDERING FOR VIEW SYNTHESIS

This task follows the original problem setup in (Tancik et al., 2020). We aim to learn an implicit representation of a 3D scene from 2D photographs using Neural Radiance Field (NeRF) (Mildenhall et al., 2020), which is a coordinate-based MLP that takes a 3D location as input and outputs a color and volume density. The network is trained by minimizing a rendering loss between the set of 2D

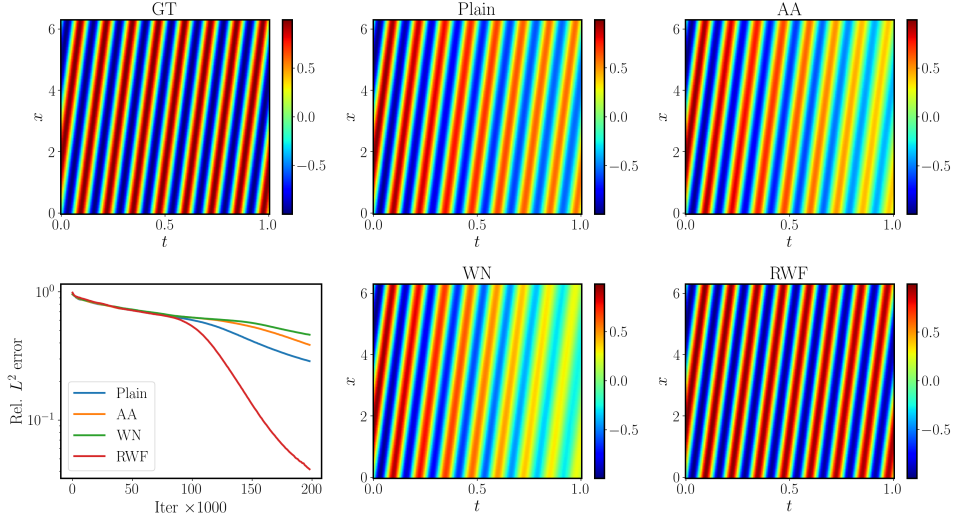


Figure 3: *Advection*: Predicted solutions of trained MLPs with different weight parameterizations, along with the evolution of the associated relative L^2 prediction errors during training.

image observations and the same rendered views from the predicted scene representation. In our experiments, we consider a down-sampled NeRF *Lego* data-set and use a simplified version of the method described in (Mildenhall et al., 2020), where we remove hierarchical sampling and view dependence. We compare the PSNR of the trained MLPs with different weight parametrizations.

4.5 SOLVING PARTIAL DIFFERENTIAL EQUATIONS (PDEs)

Our goal is to solve partial differential equations (PDEs) using physics-informed neural network (PINNs) (Raissi et al., 2019), which take the coordinates of a spatio-temporal domain as inputs and predict the corresponding target solution function. PINNs are trained in a self-supervised fashion by minimizing a composite loss function for fitting given initial and boundary conditions, as well as satisfying the underlying PDE constraints. We consider two benchmarks, an advection equation modeling the transport of a scalar field, and the Navier-Stokes equation modeling the motion of an incompressible fluid in a square cavity. Detailed descriptions and implementations of each problem are provided below and in the Appendix K.

Figure 3 and Figure 4 present the ground truth against the predicted solutions obtained by training PINNs with different weight parameterizations. It can be observed that the predictions obtained by RWF are in excellent agreement with the ground truth, while the other three parameterizations result in poor or even non-physical approximations. The rapid decrease in the test error further validates the benefit of our method. We attribute these significant performance improvements to the fact that PINN models, due to their self-supervised nature, often suffer from poor initializations. Evidently, RWF can precisely mitigate this by being able to reach better local minima that are located further away from the model initialization neighborhood.

Advection equation: The first example is 1D advection equation, a linear hyperbolic equation commonly used to model transport phenomena

$$\frac{\partial u}{\partial t} + c \frac{\partial u}{\partial x} = 0, \quad x \in (0, 2\pi), t \in [0, 1], \quad (4.1)$$

$$u(x, 0) = g(x), \quad x \in (0, 2\pi), \quad (4.2)$$

with periodic boundary conditions. This example has been studied in (Krishnapriyan et al., 2021; Daw et al., 2022), exposing some of the limitations that PINNs suffer from as the transport velocity c is increased. In our experiments, we consider $c = 50$ and an initial condition $g(x) = \sin(x)$.

Navier-Stokes equation: The second example is a classical benchmark problem in computational fluid dynamics, describing the motion of an incompressible fluid in a two-dimensional lid-driven

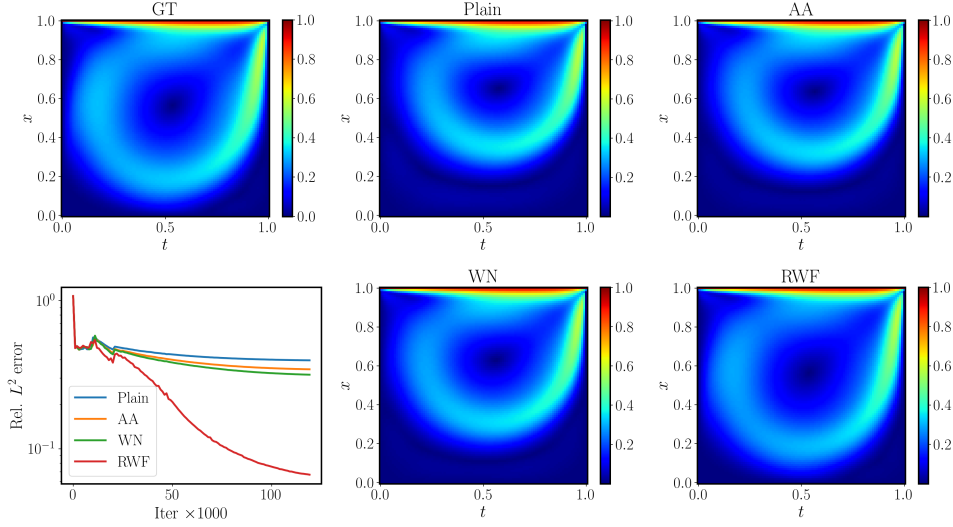


Figure 4: *Navier-Stokes*: Predicted solutions of trained MLPs with different weight parameterizations, along with the evolution of the associated relative L^2 errors during training.

cavity. The system is governed by the Navier–Stokes equations written in a non-dimensional form

$$\mathbf{u} \cdot \nabla \mathbf{u} + \nabla p - \frac{1}{Re} \Delta \mathbf{u} = 0, \quad (x, y) \in (0, 1)^2, \quad (4.3)$$

$$\nabla \cdot \mathbf{u} = 0, \quad (x, y) \in (0, 1)^2, \quad (4.4)$$

where $\mathbf{u} = (u, v)$ denotes the velocity in x and y directions, respectively, and p is the scalar pressure field. We assume $\mathbf{u} = (1, 0)$ on the top lid of the cavity, and a non-slip boundary condition on the other three walls. All experiments are performed with a Reynolds number of $Re = 1,000$.

4.6 LEARNING OPERATORS

In this task, we focus on learning the solution operators of parametric PDEs. To describe the problem setup in general, consider a parametric PDE of the following form

$$\mathcal{N}(\mathbf{a}, \mathbf{u}) = 0, \quad (4.5)$$

where $\mathcal{N} : \mathcal{A} \times \mathcal{U} \rightarrow \mathcal{V}$ is a linear or nonlinear differential operator between infinite-dimensional function spaces. Moreover, $\mathbf{a} \in \mathcal{A}$ denotes the PDE parameters, and $\mathbf{u} \in \mathcal{U}$ is the corresponding unknown solutions of the PDE system. The solution operator $G : \mathcal{A} \rightarrow \mathcal{U}$ is given by

$$G(\mathbf{a}) = \mathbf{u}(\mathbf{a}). \quad (4.6)$$

In our experiments, we consider three benchmarks: Diffusion-reaction, Darcy flow and the Burgers' equation. Detailed descriptions of each problem setup are shown below. As shown in Figure 5, we plot the training losses of each model with different weight parameterizations. One can see that *random weight factorization* yields the best loss convergence for every example, indicating the capability of the proposed method to accelerate the convergence of stochastic gradient descent and achieve better local minima.

Diffusion-reaction: Our first example involves a nonlinear diffusion-reaction PDE with a source term $a : (0, 1) \rightarrow \mathbb{R}$,

$$\frac{\partial u}{\partial t} = D \frac{\partial^2 u}{\partial x^2} + ku^2 + a(x), \quad (x, t) \in (0, 1) \times (0, 1], \quad (4.7)$$

with the zero initial and boundary conditions, where $D = 0.01$ is the diffusion coefficient and $k = 0.01$ is the reaction rate. We train a Deep Operator Network (DeepONet) Lu et al. (2021) to learn the solution operator for mapping source terms $a(x)$ to the corresponding PDE solutions $u(x)$. This network takes a PDE parameter and a spatial-temporal coordinate as inputs, and predicts the associated PDE solution evaluated at that location. The model is trained in a supervised manner by minimizing a loss between the predicted PDE solutions and the available solution measurements.

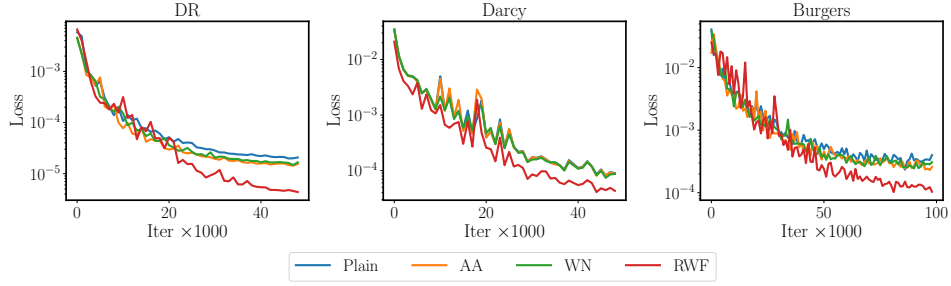


Figure 5: *Learning operators*: Loss convergence of training DeepONets with different weight parameterizations for diffusion-reaction equation, Darcy flow and the Burgers’ equation.

Darcy flow: The Darcy equation describes steady-state flow through a porous medium, taking the following form in two spatial dimensions

$$-\nabla \cdot (a \cdot \nabla u) = f, \quad (x, y) \in (0, 1)^2, \quad (4.8)$$

$$u = 0, \quad (x, y) \in \partial(0, 1)^2, \quad (4.9)$$

where $a : (0, 1) \rightarrow \mathbb{R}^+$ is the diffusion coefficient and $f : (0, 1) \rightarrow \mathbb{R}$ is a forcing term. This is a linear second-order elliptic PDE with numerous applications in modeling subsurface flow, porous media, elastic materials, etc. We fix $f(x, y) = 1$ and aim to learn a continuous representation of the solution operator $G : a(x, y) \rightarrow u(x, y)$ with a DeepONet.

Burgers’ equation: As the last example, we consider a fundamental nonlinear PDE, the one-dimensional viscous Burgers’ equation. This equation arises in various areas of applied mathematics, such as gas dynamics, nonlinear acoustics, and fluid mechanics. It takes the form

$$\frac{\partial u}{\partial t} + u \frac{\partial u}{\partial x} = \nu \frac{\partial^2 u}{\partial x^2}, \quad (x, t) \in (0, 1) \times (0, 1], \quad (4.10)$$

$$u(x, 0) = 0, \quad x \in (0, 1), \quad (4.11)$$

$$(4.12)$$

with periodic boundary conditions and $\nu = 0.001$. Our goal is to learn the solution operator from the initial condition to the associated PDE solution with a physics-informed DeepONet (Wang et al., 2021e). Different from the first two examples, the physics-informed DeepONet is trained in a self-supervised manner, i.e. without any paired input-output observations, except for a set of given initial or boundary conditions (see Wang et al. (2021e) for more details).

5 CONCLUSIONS

In this work, we proposed *random weight factorization*, a simple and remarkably effective reparameterization of the weight matrices in neural networks. Theoretically, we show how this factorization alters the geometry of a loss landscape by assigning a self-adaptive learning rate to each neuron. Empirically, we show that our method can mitigate spectral bias in MLPs and enable networks to search for good local optima further away from their initialization. We validate *random weight factorization* using six different benchmarks ranging from image regression to learning operators, showcasing a consistent and robust improvements across various tasks in computer vision, graphics, and scientific computing. These findings provide new insights into the training of continuous neural representations and open several exciting avenues for future work, including the application of our method to deep learning models beyond coordinate-based MLPs, such as convolutional networks (LeCun et al., 1998), graph networks (Scarselli et al., 2008), and Transformers (Vaswani et al., 2017).

AUTHOR CONTRIBUTIONS

SW and PP conceptualized the research and designed the numerical studies. SW, JS and PP provided the theoretical analysis. SW and HW implemented the methods and conducted the numerical experiments. PP provided funding and supervised all aspects of this work. All authors discussed the results and contributed to the final manuscript.

ACKNOWLEDGMENTS

We would like to acknowledge support from the US Department of Energy under the Advanced Scientific Computing Research program (grant DE-SC0019116), the US Air Force (grant AFOSR FA9550-20-1-0060), and US Department of Energy/Advanced Research Projects Agency (grant DE-AR0001201). We also thank the developers of the software that enabled our research, including JAX (Bradbury et al., 2018), JAX-Flax(Heek et al., 2020), Matplotlib (Hunter, 2007), and NumPy (Harris et al., 2020).

REFERENCES

- Eirikur Agustsson and Radu Timofte. Ntire 2017 challenge on single image super-resolution: Dataset and study. In *Proceedings of the IEEE conference on computer vision and pattern recognition workshops*, pp. 126–135, 2017.
- Jimmy Lei Ba, Jamie Ryan Kiros, and Geoffrey E Hinton. Layer normalization. *arXiv preprint arXiv:1607.06450*, 2016.
- Alberto Bietti and Julien Mairal. On the inductive bias of neural tangent kernels. *Advances in Neural Information Processing Systems*, 32, 2019.
- James Bradbury, Roy Frostig, Peter Hawkins, Matthew James Johnson, Chris Leary, Dougal Maclaurin, George Necula, Adam Paszke, Jake VanderPlas, Skye Wanderman-Milne, and Qiao Zhang. JAX: composable transformations of Python+NumPy programs, 2018. URL <http://github.com/google/jax>.
- Yuan Cao, Zhiying Fang, Yue Wu, Ding-Xuan Zhou, and Quanquan Gu. Towards understanding the spectral bias of deep learning. *arXiv preprint arXiv:1912.01198*, 2019.
- Zhiqin Chen and Hao Zhang. Learning implicit fields for generative shape modeling. In *Proceedings of the IEEE/CVF Conference on Computer Vision and Pattern Recognition*, pp. 5939–5948, 2019.
- Steven M Cox and Paul C Matthews. Exponential time differencing for stiff systems. *Journal of Computational Physics*, 176(2):430–455, 2002.
- Arka Daw, Jie Bu, Sifan Wang, Paris Perdikaris, and Anuj Karpatne. Rethinking the importance of sampling in physics-informed neural networks. *arXiv preprint arXiv:2207.02338*, 2022.
- Suchuan Dong and Naxian Ni. A method for representing periodic functions and enforcing exactly periodic boundary conditions with deep neural networks. *Journal of Computational Physics*, 435: 110242, 2021.
- Tobin A Driscoll, Nicholas Hale, and Lloyd N Trefethen. Chebfun guide, 2014.
- Kyle Genova, Forrester Cole, Daniel Vlasic, Aaron Sarna, William T Freeman, and Thomas Funkhouser. Learning shape templates with structured implicit functions. In *Proceedings of the IEEE/CVF International Conference on Computer Vision*, pp. 7154–7164, 2019.
- Kyle Genova, Forrester Cole, Avneesh Sud, Aaron Sarna, and Thomas Funkhouser. Local deep implicit functions for 3d shape. In *Proceedings of the IEEE/CVF Conference on Computer Vision and Pattern Recognition*, pp. 4857–4866, 2020.
- Xavier Glorot and Yoshua Bengio. Understanding the difficulty of training deep feedforward neural networks. In *Proceedings of the thirteenth international conference on artificial intelligence and statistics*, pp. 249–256, 2010.

- Charles R Harris, K Jarrod Millman, Stéfan J van der Walt, Ralf Gommers, Pauli Virtanen, David Cournapeau, Eric Wieser, Julian Taylor, Sebastian Berg, Nathaniel J Smith, et al. Array programming with numpy. *Nature*, 585(7825):357–362, 2020.
- Jonathan Heek, Anselm Levskaya, Avital Oliver, Marvin Ritter, Bertrand Rondepierre, Andreas Steiner, and Marc van Zee. Flax: A neural network library and ecosystem for JAX, 2020. URL <http://github.com/google/flax>.
- Philipp Henzler, Niloy J Mitra, and Tobias Ritschel. Learning a neural 3d texture space from 2d exemplars. In *Proceedings of the IEEE/CVF Conference on Computer Vision and Pattern Recognition*, pp. 8356–8364, 2020.
- John D Hunter. Matplotlib: A 2D graphics environment. *IEEE Annals of the History of Computing*, 9(03):90–95, 2007.
- Sergey Ioffe and Christian Szegedy. Batch normalization: Accelerating deep network training by reducing internal covariate shift. In *International conference on machine learning*, pp. 448–456. PMLR, 2015.
- Arthur Jacot, Franck Gabriel, and Clément Hongler. Neural tangent kernel: Convergence and generalization in neural networks. In *Advances in neural information processing systems*, pp. 8571–8580, 2018.
- Ameya D Jagtap, Kenji Kawaguchi, and George Em Karniadakis. Adaptive activation functions accelerate convergence in deep and physics-informed neural networks. *Journal of Computational Physics*, 404:109136, 2020.
- George Em Karniadakis, Ioannis G Kevrekidis, Lu Lu, Paris Perdikaris, Sifan Wang, and Liu Yang. Physics-informed machine learning. *Nature Reviews Physics*, pp. 1–19, 2021.
- Diederik P Kingma and Jimmy Ba. Adam: A method for stochastic optimization. *arXiv preprint arXiv:1412.6980*, 2014.
- Aditi S Krishnapriyan, Amir Gholami, Shandian Zhe, Robert M Kirby, and Michael W Mahoney. Characterizing possible failure modes in physics-informed neural networks. *arXiv preprint arXiv:2109.01050*, 2021.
- Yann LeCun, Léon Bottou, Yoshua Bengio, and Patrick Haffner. Gradient-based learning applied to document recognition. *Proceedings of the IEEE*, 86(11):2278–2324, 1998.
- Sook-Lei Liew, Julia M Anglin, Nick W Banks, Matt Sondag, Kaori L Ito, Hosung Kim, Jennifer Chan, Joyce Ito, Connie Jung, Nima Khoshab, et al. A large, open source dataset of stroke anatomical brain images and manual lesion segmentations. *Scientific data*, 5(1):1–11, 2018.
- Lu Lu, Pengzhan Jin, Guofei Pang, Zhongqiang Zhang, and George Em Karniadakis. Learning nonlinear operators via DeepONet based on the universal approximation theorem of operators. *Nature Machine Intelligence*, 3(3):218–229, 2021.
- Lars Mescheder, Michael Oechsle, Michael Niemeyer, Sebastian Nowozin, and Andreas Geiger. Occupancy networks: Learning 3d reconstruction in function space. In *Proceedings of the IEEE/CVF conference on computer vision and pattern recognition*, pp. 4460–4470, 2019.
- Ben Mildenhall, Pratul P Srinivasan, Matthew Tancik, Jonathan T Barron, Ravi Ramamoorthi, and Ren Ng. Nerf: Representing scenes as neural radiance fields for view synthesis. In *European conference on computer vision*, pp. 405–421. Springer, 2020.
- Anh Nguyen, Jason Yosinski, and Jeff Clune. Deep neural networks are easily fooled: High confidence predictions for unrecognizable images. In *Proceedings of the IEEE conference on computer vision and pattern recognition*, pp. 427–436, 2015.
- Michael Niemeyer, Lars Mescheder, Michael Oechsle, and Andreas Geiger. Differentiable volumetric rendering: Learning implicit 3d representations without 3d supervision. In *Proceedings of the IEEE/CVF Conference on Computer Vision and Pattern Recognition*, pp. 3504–3515, 2020.

- Michael Oechsle, Lars Mescheder, Michael Niemeyer, Thilo Strauss, and Andreas Geiger. Texture fields: Learning texture representations in function space. In *Proceedings of the IEEE/CVF International Conference on Computer Vision*, pp. 4531–4540, 2019.
- Jeong Joon Park, Peter Florence, Julian Straub, Richard Newcombe, and Steven Lovegrove. DeepSDF: Learning continuous signed distance functions for shape representation. In *Proceedings of the IEEE/CVF Conference on Computer Vision and Pattern Recognition*, pp. 165–174, 2019.
- Nasim Rahaman, Aristide Baratin, Devansh Arpit, Felix Draxler, Min Lin, Fred Hamprecht, Yoshua Bengio, and Aaron Courville. On the spectral bias of neural networks. In *International Conference on Machine Learning*, pp. 5301–5310, 2019.
- Maziar Raissi, Paris Perdikaris, and George E Karniadakis. Physics-informed neural networks: A deep learning framework for solving forward and inverse problems involving nonlinear partial differential equations. *Journal of Computational Physics*, 378:686–707, 2019.
- Maziar Raissi, Alireza Yazdani, and George Em Karniadakis. Hidden fluid mechanics: Learning velocity and pressure fields from flow visualizations. *Science*, 367(6481):1026–1030, 2020.
- Shunsuke Saito, Zeng Huang, Ryota Natsume, Shigeo Morishima, Angjoo Kanazawa, and Hao Li. Pifu: Pixel-aligned implicit function for high-resolution clothed human digitization. In *Proceedings of the IEEE/CVF International Conference on Computer Vision*, pp. 2304–2314, 2019.
- Tim Salimans and Durk P Kingma. Weight normalization: A simple reparameterization to accelerate training of deep neural networks. *Advances in neural information processing systems*, 29, 2016.
- Franco Scarselli, Marco Gori, Ah Chung Tsoi, Markus Hagenbuchner, and Gabriele Monfardini. The graph neural network model. *IEEE transactions on neural networks*, 20(1):61–80, 2008.
- Lawrence A Shepp and Benjamin F Logan. The fourier reconstruction of a head section. *IEEE Transactions on nuclear science*, 21(3):21–43, 1974.
- Vincent Sitzmann, Michael Zollhöfer, and Gordon Wetzstein. Scene representation networks: Continuous 3d-structure-aware neural scene representations. *Advances in Neural Information Processing Systems*, 32, 2019.
- Vincent Sitzmann, Julien Martel, Alexander Bergman, David Lindell, and Gordon Wetzstein. Implicit neural representations with periodic activation functions. *Advances in Neural Information Processing Systems*, 33:7462–7473, 2020.
- Kenneth O Stanley. Compositional pattern producing networks: A novel abstraction of development. *Genetic programming and evolvable machines*, 8(2):131–162, 2007.
- Matthew Tancik, Pratul P Srinivasan, Ben Mildenhall, Sara Fridovich-Keil, Nithin Raghavan, Utkarsh Singhal, Ravi Ramamoorthi, Jonathan T Barron, and Ren Ng. Fourier features let networks learn high frequency functions in low dimensional domains. *arXiv preprint arXiv:2006.10739*, 2020.
- Ashish Vaswani, Noam Shazeer, Niki Parmar, Jakob Uszkoreit, Llion Jones, Aidan N Gomez, Łukasz Kaiser, and Illia Polosukhin. Attention is all you need. *Advances in neural information processing systems*, 30, 2017.
- Hanwen Wang, Isabelle Crawford-Eng, and Paris Perdikaris. Enhancing the trainability and expressivity of deep MLPs with globally orthogonal initialization. In *The Symbiosis of Deep Learning and Differential Equations*, 2021a. URL <https://openreview.net/forum?id=KkMGjzTsXM>.
- Sifan Wang, Yujun Teng, and Paris Perdikaris. Understanding and mitigating gradient flow pathologies in physics-informed neural networks. *SIAM Journal on Scientific Computing*, 43(5):A3055–A3081, 2021b.

- Sifan Wang, Hanwen Wang, and Paris Perdikaris. On the eigenvector bias of fourier feature networks: From regression to solving multi-scale PDEs with physics-informed neural networks. *Computer Methods in Applied Mechanics and Engineering*, 384:113938, 2021c.
- Sifan Wang, Hanwen Wang, and Paris Perdikaris. Improved architectures and training algorithms for deep operator networks. *arXiv preprint arXiv:2110.01654*, 2021d.
- Sifan Wang, Hanwen Wang, and Paris Perdikaris. Learning the solution operator of parametric partial differential equations with physics-informed deepnets. *Science advances*, 7(40):eabi8605, 2021e.
- Sifan Wang, Shyam Sankaran, and Paris Perdikaris. Respecting causality is all you need for training physics-informed neural networks. *arXiv preprint arXiv:2203.07404*, 2022.
- Zhi-Qin John Xu, Yaoyu Zhang, Tao Luo, Yanyang Xiao, and Zheng Ma. Frequency principle: Fourier analysis sheds light on deep neural networks. *arXiv preprint arXiv:1901.06523*, 2019.

A PROOFS

A.1 PROOF OF THEOREM 1

Proof. Note that for any pair $(\mathbf{s}^{(l)}, \mathbf{V}^{(l)})$ with $\text{diag}(\mathbf{s}^{(l)}) \cdot \mathbf{V}^{(l)} = \mathbf{W}^{(l)}$, we have

$$\|\mathbf{V}^{(l)}\| \rightarrow 0, \text{ as } \mathbf{s}^{(l)} \rightarrow \infty \quad (\text{A.1})$$

for $l = 1, 2, \dots, L+1$. Then for any $\epsilon > 0$, there exists $M > 0$ such that for any $(\mathbf{V}^{(l)}, \mathbf{s}^{(l)})_{l=1}^{L+1} \in U_{\boldsymbol{\theta}}$, and $\|\mathbf{s}^{(l)}\| > M$, we obtain $\|\mathbf{V}^{(l)}\| < \epsilon$, for $l = 1, 2, \dots, L+1$. We define U_* by

$$U_* = \{(\mathbf{0}, \mathbf{s}^{(l)})_{l=1}^{L+1} : \mathbf{s}^{(l)} \in \mathbb{R}^{d_l}, l = 1, 2, \dots, L+1\} \quad (\text{A.2})$$

Now we can choose $\mathbf{s}^{(l)}$ such that $\|\mathbf{s}^{(l)}\| > M$. Then

$$\text{dist}(U_{\boldsymbol{\theta}}, U_*) \leq \sqrt{\sum_{l=1}^{L+1} \|\mathbf{V}^{(l)}\|^2} \leq \sqrt{L+1} \epsilon \quad (\text{A.3})$$

Similarly, we can show that

$$\text{dist}(U_{\boldsymbol{\theta}'}, U_*) \leq \sqrt{\sum_{l=1}^{L+1} \|\mathbf{V}^{(l)}\|^2} \leq \sqrt{L+1} \epsilon \quad (\text{A.4})$$

Therefore,

$$\text{dist}(U_{\boldsymbol{\theta}}, U_{\boldsymbol{\theta}'}) \leq \text{dist}(U_{\boldsymbol{\theta}}, U_*) + \text{dist}(U_*, U_{\boldsymbol{\theta}'}) \leq 2\sqrt{L+1} \epsilon \quad (\text{A.5})$$

Since ϵ is arbitrary, letting $\epsilon \rightarrow 0$ gives

$$\text{dist}(U_{\boldsymbol{\theta}}, U_{\boldsymbol{\theta}'}) = 0. \quad (\text{A.6})$$

□

A.2 PROOF OF THEOREM 2

Proof. Suppose that $f^{(k,l)}$ denotes k -th component of $\mathbf{f}^{(l)} \in \mathbb{R}^{d_l}$. Under the proposed weight factorization in equation 2.3, differentiating the loss function \mathcal{L} with respect to $\mathbf{w}^{(k,l)}$ and $\mathbf{s}^{(k,l)}$, respectively, yields

$$\mathbf{s}_{n+1}^{(k,l)} = \mathbf{s}_n^{(k,l)} - \eta \frac{\partial \mathcal{L}}{\partial \mathbf{s}_n^{(k,l)}} = \mathbf{s}_n^{(k,l)} - \eta \frac{\partial \mathcal{L}}{\partial f^{(k,l)}} \cdot \mathbf{v}_n^{(k,l)} \cdot \mathbf{g}^{(l-1)}, \quad (\text{A.7})$$

$$\mathbf{v}_{n+1}^{(k,l)} = \mathbf{v}_n^{(k,l)} - \eta \frac{\partial \mathcal{L}}{\partial \mathbf{v}_n^{(k,l)}} = \mathbf{v}_n^{(k,l)} - \eta \mathbf{s}_n^{(k,l)} \frac{\partial \mathcal{L}}{\partial f^{(k,l)}} \cdot \mathbf{g}^{(l-1)}. \quad (\text{A.8})$$

Note that

$$\frac{\partial \mathcal{L}}{\partial \mathbf{w}_n^{(k,l)}} = \frac{\partial \mathcal{L}}{\partial f^{(k,l)}} \cdot \mathbf{g}^{(l-1)}, \quad (\text{A.9})$$

and the update rule of $\mathbf{v}^{(k,l)}$ and $\mathbf{s}^{(k,l)}$ can be re-written as

$$\mathbf{s}_{n+1}^{(k,l)} = \mathbf{s}_n^{(k,l)} - \eta \mathbf{v}_n^{(k,l)} \cdot \frac{\partial \mathcal{L}}{\partial \mathbf{w}_n^{(k,l)}}, \quad (\text{A.10})$$

$$\mathbf{v}_{n+1}^{(k,l)} = \mathbf{v}_n^{(k,l)} - \eta \mathbf{s}_n^{(k,l)} \frac{\partial \mathcal{L}}{\partial \mathbf{w}_n^{(k,l)}}. \quad (\text{A.11})$$

Since $\mathbf{w}^{(k,l)} = \mathbf{s}^{(k,l)} \cdot \mathbf{v}^{(k,l)}$, the update rule of $\mathbf{w}^{(k,l)}$ is given by

$$\mathbf{w}_{n+1}^{(k,l)} = \mathbf{w}_n^{(k,l)} - \eta \left(\|\mathbf{s}_n^{(k,l)} + \mathbf{v}_n^{(k,l)}\|_2^2 \right) \frac{\partial \mathcal{L}}{\partial \mathbf{w}_n^{(k,l)}} + \mathcal{O}(\eta^2) \quad (\text{A.12})$$

□

B ALGORITHM OF RANDOM WEIGHT FACTORIZATION

Algorithm 1 Random weight factorization (RWF)

1. Initialize a neural network f_{θ} with $\theta = \{\mathbf{W}^{(l)}, \mathbf{b}^{(l)}\}_{l=1}^{L+1}$ (e.g. using the Glorot scheme (Glorot & Bengio, 2010)).
 - for** $l = 1, 2, \dots, L$ **do**
 - (a) Initialize each scale factor as $\mathbf{s}^{(l)} \sim \mathcal{N}(\mu, \sigma I)$.
 - (b) Construct the factorized weight matrices as $\mathbf{W}^{(l)} = \text{diag}(\exp(\mathbf{s}^{(l)})) \cdot \mathbf{V}^{(l)}$.
 - end for**
 2. Train the network by gradient descent on the factorized parameters $\{\mathbf{s}^{(l)}, \mathbf{V}^{(l)}, \mathbf{b}^{(l)}\}_{l=1}^{L+1}$. The recommended hyper-parameters are $\mu = 1.0, \sigma = 0.1$.
-

C A DROP-IN ENHANCEMENT FOR LINEAR LAYERS

```

1 class Dense(nn.Module):
2     features: int
3
4     @nn.compact
5     def __call__(self, x):
6         kernel = self.param('kernel',
7                               glorot_normal(),
8                               (x.shape[-1],
9                                self.features))
10        bias = self.param('bias',
11                           nn.initializers.zeros,
12                           (self.features,))
13        y = np.dot(x, kernel) + bias
14        return y

```

Listing 1: JAX Flax implementation (Heek et al., 2020) of a conventional linear layer.

```

1 def factorized_glorot_normal(mean=1.0, stddev=0.1):
2     def init(key, shape):
3         key1, key2 = random.split(key)
4         w = glorot_normal()(key1, shape)
5         s = mean + normal(stddev)(key2, (shape[-1],))
6         s = np.exp(s)
7         v = w / s
8         return s, v
9     return init
10
11 class FactorizedDense(nn.Module):
12     features: int
13
14     @nn.compact
15     def __call__(self, x):
16         s, v = self.param('kernel',
17                           factorized_glorot_normal(),
18                           (x.shape[-1], self.features))
19         kernel = s * v
20         bias = self.param('bias',
21                           nn.initializers.zeros,
22                           (self.features,))
23         y = np.dot(x, kernel) + bias
24         return y

```

Listing 2: JAX Flax implementation (Heek et al., 2020) of a linear layer with *random weight factorization*.

D 1D REGRESSION ABLATION STUDY

We perform a systematic study on the effect of μ and σ used for initializing the scale factor s in *random weight factorization*. To this end, we train MLPs with *random weight factorization* initialized by different μ and σ . Each model (3 layers, 128 channels, ReLU activations) is trained via a full-batch gradient descent for 10^5 iterations using the Adam optimizer (Kingma & Ba, 2014) with a starting learning rate of 10^{-3} followed by an exponential decay by a factor of 0.9 in every 5,000 steps. The resulting relative L^2 errors are visualized in Figure 6. We observe that models initialized with a small μ achieve similar performance to our baseline, while large μ and σ values can lead to an unstable training process and poor predictive accuracy. In particular, $\mu = 1$ and $\sigma = 0.1$ yield the best results, and thus we will use this as the default hyper-parameter of random weight factorization in the majority of the benchmarks presented here (see Table 4).

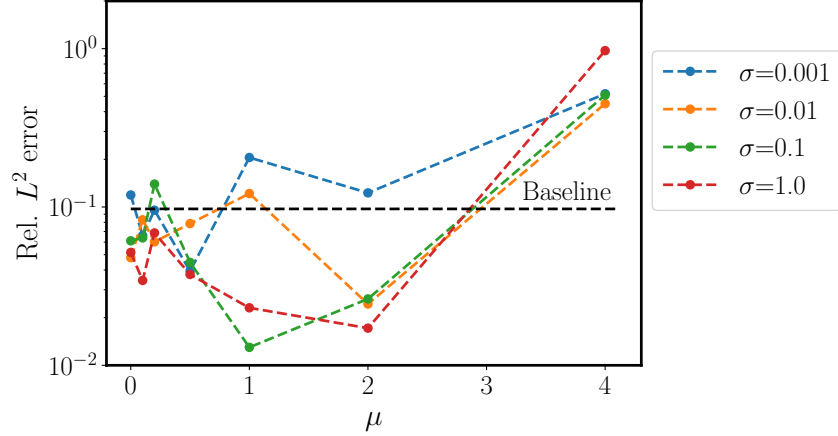


Figure 6: *1D Regression*: Resulting relative L^2 errors of training MLPs with *random weight factorization* initialized by different μ and σ . The baseline (black dash) represents the result of training a plain MLP.

E HYPER-PARAMETERS

The following tables summarizes the hyper-parameters of the different networks architectures employed in each benchmark (Table 2), their associated learning rate schedules (Table 3), and the corresponding random weight factorization settings (Table 4).

Task	Case	Backbone	Depth	width	Activation
Image Regression	Natural	MLP	4	256	ReLU
	Text				
Shape Representation	Dragon	MLP	8	256	ReLU
	Armadillo				
Computed Tomography	Shepp	MLP	5	256	ReLU
	ATLAS				
Inverse Rendering	Lego	MLP	5	256	ReLU
Solving PDEs	Advection	MLP	5	256	Tanh
	Navier-Stokes	MLP	5	128	
		Modified MLP			
Learning Operators	DR	DeepONet	5	64	Tanh
	Darcy		4	128	GELU
		Burgers	Modified DeepONet	5	128

Table 2: Network architectures for each benchmark.

Task	Case	Learning Rate Schedule				Iterations
		Step Size	Decay Steps	Decay Rate	Warmup Steps	
Image Regression	Natural	10^{-3}	-	-	2×10^2	2×10^3
	Text					
Shape Representation	Dragon	5×10^{-4}	5×10^3	0.1	10^3	10^4
	Armadillo					
Computed Tomography	Shepp	10^{-3}	-	-	2×10^2	2×10^3
	ATLAS					
Inverse Rendering	Lego	10^{-3}	10^3	0.9	5×10^3	5×10^4
Solving PDEs	Advection	10^{-3}	5×10^3	0.9	-	2×10^5
	Navier-Stokes		2×10^3	0.9		1.2×10^5
Learning Operators	DR	10^{-3}	10^3	0.9	-	5×10^4
	Darcy					
	Burgers		2×10^3	0.9		10^5

Table 3: Learning Rate Schedules for each benchmark.

Task	Case	Initialization of RWF
Image Regression	Natural	$s \sim \mathcal{N}(2, 0.01)$
	Text	$s \sim \mathcal{N}(1, 0.1)$
Shape Representation	Dragon	$s \sim \mathcal{N}(1, 0.1)$
	Armadillo	
Computed Tomography	Shepp	$s \sim \mathcal{N}(1, 0.1)$
	ATLAS	
Inverse Rendering	Lego	$s \sim \mathcal{N}(1, 0.1)$
Solving PDEs	Advection	$s \sim \mathcal{N}(1, 0.1)$
	Navier-Stokes	$s \sim \mathcal{N}(0.5, 0.1)$
Learning Operators	DR	$s \sim \mathcal{N}(1, 0.1)$
	Darcy	
	Burgers	

Table 4: Distribution used for initializing the scale factor in *random weight factorization*.

F COMPUTATIONAL COSTS

Table 5 presents the computational cost in terms of training iterations per second for the networks employed in each benchmark. All timings are reported on a single NVIDIA RTX A6000 GPU.

Task	Case	Plain	AA	WN	RWF
Image Regression	Natural	116.36	111.33	114.09	113.80
	Text	116.86	112.04	113.77	113.99
Shape Representation	Dragon	12.79	12.79	12.76	12.73
	Armadillo	13.14	13.06	12.81	12.94
Computed Tomography	Shepp	30.02	29.21	29.83	29.88
	ATLAS	29.47	28.74	29.36	29.32
Inverse Rendering	Lego	30.59	29.41	30.68	30.75
Solving PDEs	Advection	853.82	757.19	855.50	789.41
	Navier-Stokes	164.02	152.70	160.51	160.45
Learning Operators	DR	469.09	450.44	470.34	469.00
	Darcy	63.10	61.21	62.92	62.91
	Burgers	27.86	26.25	27.29	27.10

Table 5: Computational cost (training iterations per second) for each benchmark. We can see that the computational overhead of *random weight factorization* is marginal.

G 2D IMAGE REGRESSION

As mentioned in Section 4.1, we use two image data-sets: *Natural* and *Natural*. All the test images have a 512×512 resolution while the training data has a 256×256 resolution. For each data-set, we compare the performance of MLPs with different parameterizations (see 2.3) and the following input embeddings:

No mapping: MLP with no input feature mapping.

Positional encoding (Tancik et al., 2020): $\gamma(\mathbf{x}) = [\dots, \cos(2\pi\sigma^{j/m}\mathbf{x}), \sin(2\pi\sigma^{j/m}\mathbf{x}), \dots]^T$ for $j = 0, 1, \dots, m-1$. where the frequencies are log-linear spaced and the scale $\sigma > 0$ is a user-specified hyper-parameter.

Gaussian (Tancik et al., 2020): $\gamma(\mathbf{x}) = [\cos(2\pi\mathbf{B}\mathbf{x}), \sin(2\pi\mathbf{B}\mathbf{x})]^T$, where $\mathbf{B} \in \mathbb{R}^{m \times d}$ is sampled from a Gaussian distribution $\mathcal{N}(0, \sigma^2)$. The scale $\sigma > 0$ is a user-specified hyper-parameter.

Each model (4 layers, 256 channels, ReLU activations) is trained via a full-batch gradient descent for 2,000 iterations using the Adam optimizer (Kingma & Ba, 2014) with default settings and 200 warm-up steps. Particularly, the mapping scales of positional encoding and Gaussian Fourier features are the same as in (Tancik et al., 2020). For random weight factorization, we initialize the scale factor $\mathbf{s} \sim \mathcal{N}(2, 0.01)$ and $\mathbf{s} \sim \mathcal{N}(1, 0.01)$ for the *Natural* and *Text* data-set, respectively. The resulting test PSNR is reported in Table 6 and Table 7. We can see that the weight factorization with Gaussian Fourier features achieves the best PSNR among all the cases. Some visualizations are shown in Figure 7 and Figure 8.

<i>Natural</i> data-set	Plain	AA	WN	RWF (ours)
No mapping	17.94 ± 2.38	18.29 ± 2.44	18.28 ± 2.44	19.11 ± 2.50
Positional Encoding	27.04 ± 3.89	26.73 ± 3.67	26.99 ± 3.83	27.46 ± 3.82
Gaussian	27.35 ± 4.05	27.36 ± 3.96	27.36 ± 4.03	28.08 ± 4.34

Table 6: *2D Image Regression*: Mean and standard deviation of PSNR obtained by training MLPs with different input mappings and weight parameterizations for the *Natural* data-set.

<i>Text</i> data-set	Plain	AA	WN	RWF (ours)
No mapping	18.42 ± 2.42	18.43 ± 2.34	18.46 ± 2.31	17.85 ± 2.36
Positional encoding	31.33 ± 2.71	31.73 ± 2.29	31.43 ± 2.57	30.49 ± 2.45
Gaussian	32.09 ± 1.80	32.29 ± 1.99	32.25 ± 1.74	33.13 ± 2.03

Table 7: *2D Image Regression*: Mean and standard deviation of PSNR obtained by training MLPs with different input mappings and weight parameterizations for the *Text* data-set.



Figure 7: *2D Image Regression*: Predicted *Natural* images of trained MLPs with Gaussian Fourier features and with different weight parameterizations.

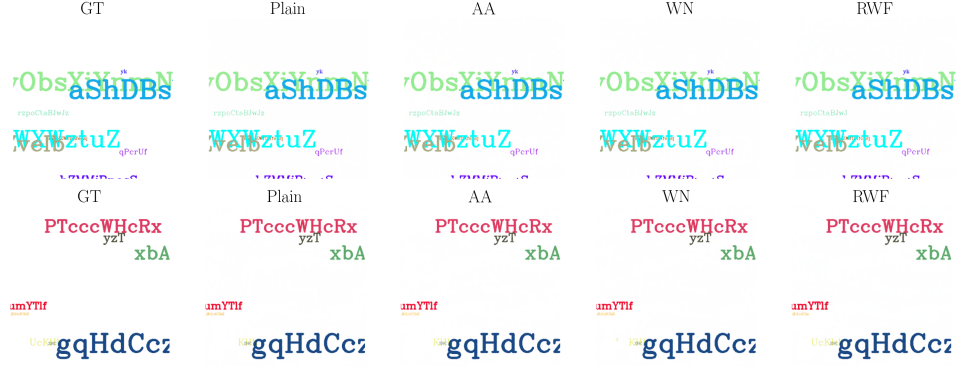


Figure 8: *2D Image Regression*: Predicted *Text* images of trained MLPs with Gaussian Fourier features and with different weight parameterizations.

Comparison with SIREN (Sitzmann et al., 2020): We find that SIREN also factorizes the weight matrix of every hidden layer as $W = \omega_0 \times \widehat{W}$ with some scale factor ω_0 . It is indeed a special case of our approach. To examine its performance, we vary the scale factor w_0 and train SIREN networks under the same hyper-parameter setting, and present the test error over the *Natural* and *Text* data-set in Figure 9. It can be observed that the scale factor w_0 plays a fundamental role in the SIREN performance. If we take $w_0 = 1$, then SIREN just performs similarly to our baseline (Plain MLP with no input mapping). Therefore, we may argue that the success of SIREN can be attributed to that simple weight factorization instead of the sine activations with the associated initialization scheme $W \sim \mathcal{U}(-\sqrt{6/d}, \sqrt{6/d})$. Nevertheless, the best PSNR that SIREN achieves is still significantly lower than the proposed random weight factorization with positional encodings or Gaussian Fourier features.

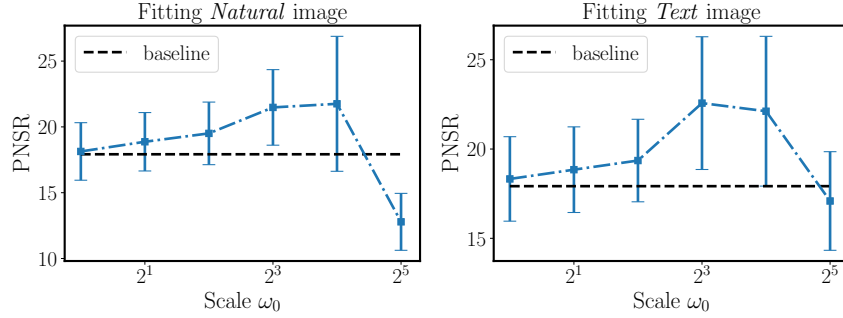


Figure 9: *2D Image Regression*: PSNR of training SIREN networks with different scale factor for the *Natural* and *Text* data-set, respectively. Error bars are plotted over different images in the data-set. The baseline (black dash) represents the result of training a plain MLP with no input mapping.

H 2D COMPUTED TOMOGRAPHY

For this task, we use two data-sets: procedurally-generated Shepp-Logan phantoms (Shepp & Logan, 1974) and 2D brain images from the ATLAS data-set (Liew et al., 2018). Each data-set consist of 20 images of 512×512 resolution. To generate the training data, we compute 20 and 40 synthetic integral projections at evenly-spaced angles for every image of *Shepp* and *ATLAS* data-set, respectively.

Similar to the previous tasks, we compare the performance of MLPs with different input mappings and weight parameterizations. In experiments, we take a scale factor $\sigma = 3$ for both positional encoding and Gaussian Fourier features and initialize $s \sim \mathcal{N}(1, 0.1)$ for using random weight factorization. Each model (5 layers, 256 channels, ReLU activations) is trained via a full-batch gradient

descent for 2,000 iteration using the the Adam optimizer (Kingma & Ba, 2014) (Kingma & Ba, 2014) with default settings and 200 warm-up steps.

Table 8 summarizes the test PSNR over *Shepp* and *ATLAS* data-set, respectively. For different input mappings, random weight factorization yields the best PSNR, consistently outperforming other parameterizations. Besides, we plot some model predictions corresponding to Gaussian input mapping in Figure 10 and 11.

<i>Shepp</i> data-set	Plain	AA	WN	RWF (ours)
No mapping	22.78 ± 1.35	23.44 ± 1.27	23.37 ± 0.84	24.39 ± 1.56
Positional encoding	29.56 ± 1.73	29.71 ± 1.80	29.87 ± 1.86	32.43 ± 1.51
Gaussian	30.08 ± 1.63	30.44 ± 1.69	30.55 ± 1.72	33.70 ± 1.29
<i>ATLAS</i> data-set	Plain	AA	WN	RWF (ours)
No mapping	15.87 ± 0.66	16.07 ± 0.68	16.17 ± 0.63	16.49 ± 0.61
Positional encoding	21.44 ± 0.94	21.54 ± 0.92	21.70 ± 0.63	23.34 ± 0.92
Gaussian	22.02 ± 0.93	22.02 ± 1.05	22.10 ± 1.04	23.61 ± 0.83

Table 8: *2D Computed Tomography*: Mean and standard deviation of PSNR obtained by training MLPs with different input mappings and weight parameterizations for the *Shepp* and *ATLAS* data-set, respectively.

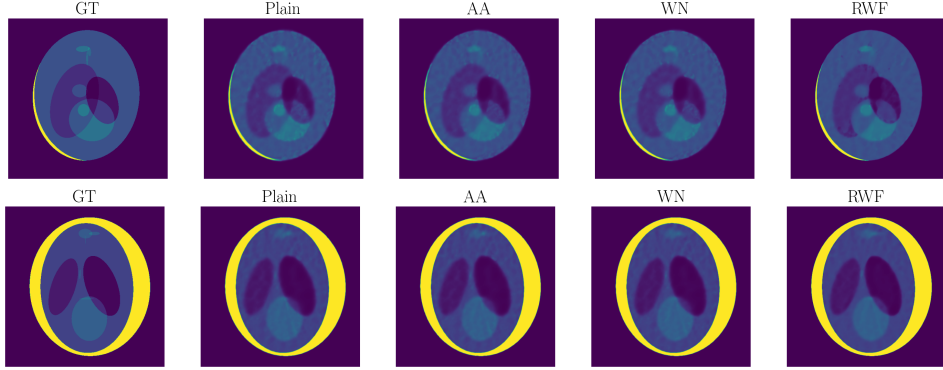


Figure 10: *2D Computed Tomography*: Predictions of trained MLPs with Gaussian Fourier features and with different weight parameterizations for the *Shepp* data-set.

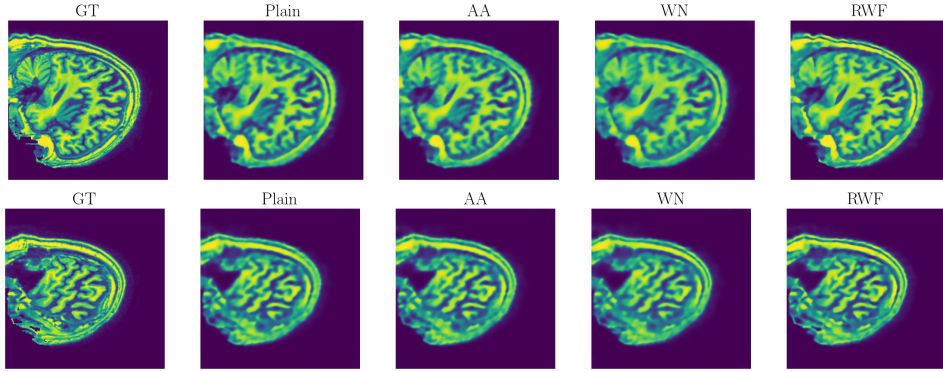


Figure 11: *2D Computed Tomography*: Predictions of trained MLPs with Gaussian Fourier features and with different weight parameterizations for the *ATLAS* data-set.

Comparison with SIREN (Sitzmann et al., 2020): We also test the performance of SIREN for this example. Specifically, we train SIREN network with different scale factor ω_0 under the same hyper-parameter settings. As shown in Figure 12, SIREN using the optimal scale factor is just slightly better than our baseline (plain MLP with no input mapping), but still worse than using positional encodings or random Fourier features.

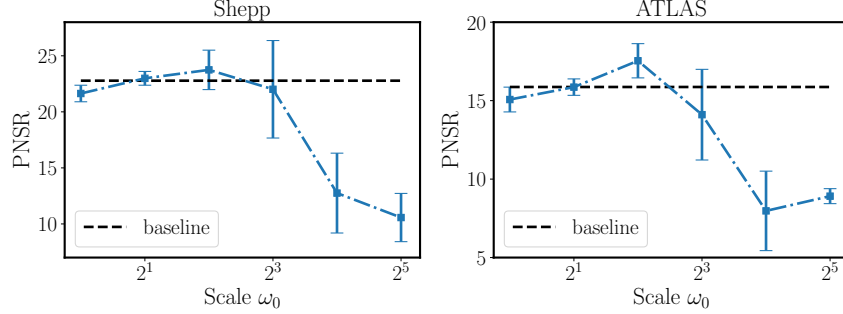


Figure 12: *2D Computed Tomography*: PSNR of training SIREN networks with different scale factor for the *Shepp* and *ATLAS* data-set, respectively. Error bars are plotted over different images in the data-set. The baseline (black dash) represents the result of training a plain MLP with no input mapping.

I 3D SHAPE REPRESENTATION

For this example, we consider two complex triangle meshes *Dragon* and *Armadillo*, both of which contain hundreds of thousands of vertices. In our experiments, every mesh is rescaled to fit inside the unit cube $[0, 1]^3$ such that the centroid of the mesh is $(0.5, 0.5, 0.5)$.

We represent each shape by MLPs with different input mappings and weight parameterizations. For models with input mappings, we use the same hyper-parameters as in (Tancik et al., 2020). For models using *random weight factorization*, we initialize the scale factor using the recommended settings $s \sim \mathcal{N}(1, 0.1)$. All networks are trained by minimizing a cross-entropy loss to match the corresponding classification labels (0 for points outside the mesh, 1 for points inside).

We train each model (8 layers, 128 channels, ReLU activations) via a mini-batch gradient descent for 10^4 iterations using the Adam optimizer (Kingma & Ba, 2014) with a start learning rate 5×10^{-4} and an exponential decay by a factor of 0.1 for every 5,000 steps. The batch size we use is 8192. To emphasize the learning of fine surface details, we calculate the test error on a set close to the mesh surface, which is generated by randomly choosing mesh vertices that have been perturbed by a random Gaussian vector with a standard deviation of 0.01.

The resulting IoU scores of each model is reported in Table 9. One can observe consistent improvements of RWF across different input mappings and data-sets, outperforming the other parameterizations. Moreover, the learned shape representations are depicted in Figure 13.

<i>Dragon</i> data-set	Plain	AA	WN	RWF (ours)
No mapping	0.894	0.894	0.891	0.924
Positional encoding	0.967	0.968	0.970	0.977
Gaussian	0.980	0.981	0.981	0.984
<i>Armadillo</i> data-set	Plain	AA	WN	RWF (ours)
No mapping	0.842	0.846	0.845	0.901
Positional encoding	0.965	0.967	0.967	0.972
Gaussian	0.978	0.976	0.975	0.982

Table 9: *3D Shape Representation*: IoU of training MLPs with different input mappings and weight parameterizations for the *Dragon* and *Armadillo* data-sets.

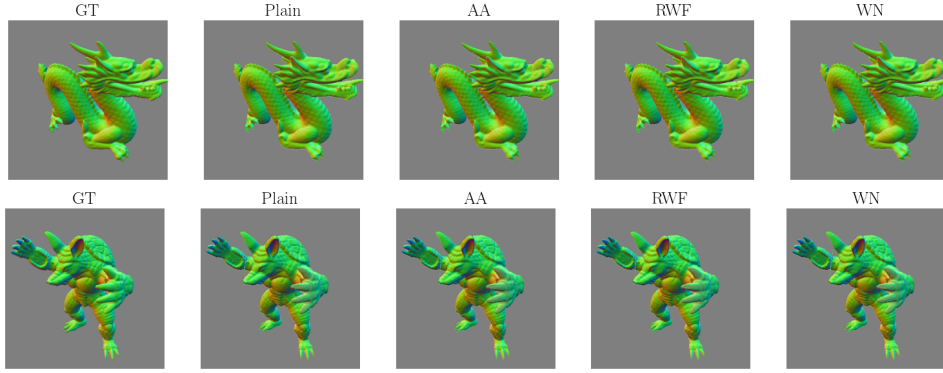


Figure 13: *3D Shape Representation*: Rendered shape representations obtained by training MLPs with Gaussian Fourier features and with different weight parameterizations.

J 3D INVERSE RENDERING FOR VIEW SYNTHESIS

For this task, we use the NeRF *Lego* data-set of 120 images downsampled to 400×400 pixel resolution. The data-set is split into 100 training images, 7 validation images, and 13 test images. In our experiments, we only use Gaussian Fourier features of a scale $\sigma = 10$, as it has been empirically validated to be the best input mapping in the previous tasks.

We train MLPs (5 layers, 256 channels, ReLU activations) with different parameterizations for 5×10^4 iterations using the Adam optimizer (Kingma & Ba, 2014) with a start learning rate of 10^{-3} and a warmup exponential decay by a factor of 0.9 for every 1,000 steps. The batch size is 2048. In Figure 14, we visualize the test PSNR of each model during training. In comparison with other three parameterizations, the MLP with RWF achieves the best PSNR. Some visualizations are provided in Figure 15

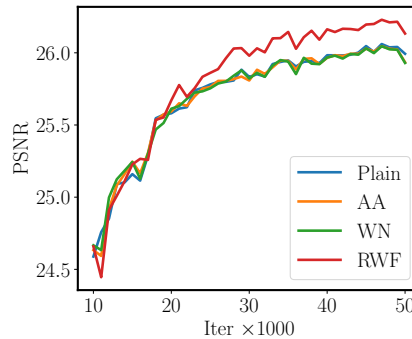


Figure 14: *3D Inverse Rendering*: Test PSNR of MLPs with different weight parameterizations during training.

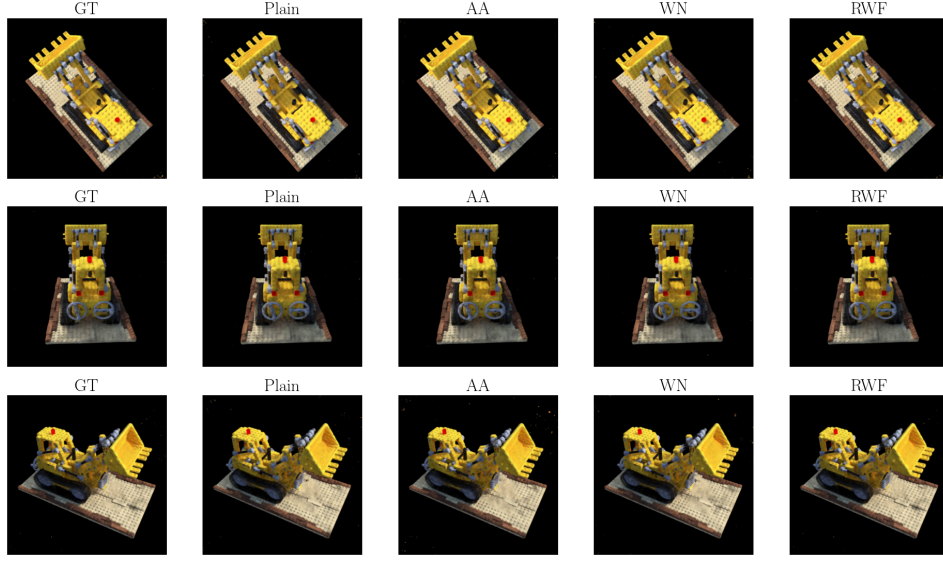


Figure 15: *3D Inverse Rendering*: Rendered views of trained MLPs with different weight parameterizations.

K SOLVING PDES

In this section, we present the implementation details of PINNs for solving advection and Navier-Stokes equation, respectively.

K.1 ADVECTION EQUATION

Recall

$$\frac{\partial u}{\partial t} + c \frac{\partial u}{\partial x} = 0, \quad x \in (0, 2\pi), t \in [0, 1] \quad (\text{K.1})$$

$$u(x, 0) = g(x), \quad x \in (0, 2\pi) \quad (\text{K.2})$$

with periodic boundary conditions and $c = 50$.

We represent the unknown solution u by an MLP u_{θ} . In particular, we impose the exact periodic boundary conditions by constructing a special Fourier feature embedding of the form (Dong & Ni, 2021)

$$\gamma(x, t) = [\cos(x), \sin(x), t]^T. \quad (\text{K.3})$$

The network can be trained by minimizing the composite loss below

$$\mathcal{L}(\theta) = \lambda_{ic} \mathcal{L}_{ic}(\theta) + \lambda_r \mathcal{L}_r(\theta) \quad (\text{K.4})$$

where

$$\mathcal{L}_{ic}(\theta) = \frac{1}{N_{ic}} \sum_{i=1}^{N_{ic}} |u_{\theta}(0, x_{ic}^i) - g(x_{ic}^i)|^2, \quad (\text{K.5})$$

$$\mathcal{L}_r(\theta) = \frac{1}{N_r} \sum_{i=1}^{N_r} \left| \frac{\partial u_{\theta}}{\partial t}(t_r^i, x_r^i) + c \frac{\partial u_{\theta}}{\partial x}(t_r^i, x_r^i) \right|^2. \quad (\text{K.6})$$

Here we set $N_{ic} = 128$ and $N_r = 1024$, and $\{x_{ic}\}_{i=1}^{N_{ic}}, \{(x_r, t_r)\}_{i=1}^{N_r}$ are randomly sampled from the computational domain, respectively, at each iteration of gradient descent. In addition, we take $\lambda_{ic} = 100, \lambda_r = 1$ for better enforcing the initial condition. It is worth pointing out that all the network derivatives are computed via automatic differentiation.

To enhance the model performance, we introduce the *curriculum* training (Krishnapriyan et al., 2021) and *causal* training (Wang et al., 2022) in the training process.

Curriculum training starts with a simple PDE system and progressively solves the target PDE system. For this example, it is accomplished by minimizing the above PINN loss with a lower advection coefficient $c = 10$ first and then gradually increasing c to the target value (i.e. $c = 50$) during training.

Causal training aims to impose temporal causality during the training of a PINNs model by appropriately re-weighting the PDE residual loss at each iteration of gradient descent. Specifically, we split the temporal domain into M chunks $[0, \Delta t]$, $[\Delta t, 2\Delta t]$, \dots , and assign a weight to the corresponding temporal residuals losses $\mathcal{L}_r^i(\boldsymbol{\theta})$ as

$$\mathcal{L}_r(\boldsymbol{\theta}) = \sum_{i=1}^M w_i \mathcal{L}_r^i(\boldsymbol{\theta}), \quad (\text{K.7})$$

with $w_1 = 1$, and

$$w_i = \exp\left(-\epsilon \sum_{k=1}^{i-1} \mathcal{L}_r^k(\boldsymbol{\theta})\right), \quad \text{for } i = 2, \dots, M. \quad (\text{K.8})$$

Here ϵ is a so-called *causal* parameter, which is a user-specified hyper-parameter that determines the slope of the causal weights. We take $M = 16$ and $\epsilon = 0.1$ in this example.

We initialize MLPs (5 layers, 256 channels, tanh activations) with different weight parameterizations, and train each model with different strategies for 2×10^5 iterations using the Adam optimizer (Kingma & Ba, 2014) with a start learning rate of 10^{-3} and an exponential decay by a factor of 0.9 for every 5,000 steps. The resulting relative L^2 errors are presented in Table 10. In contrast to the failure of the other three parameterizations, RWF is the only one that enables PINN models to solve the advection equation with a reasonable and stable predictive accuracy. Further improvements can be obtained by combining RWF with *curriculum* or *causal* training strategies. These conclusions are further clarified by the visualizations in Figures 3, 16 and 17, where the predicted solutions corresponding to RWF are in excellent agreement with the ground truth.

Advection	Plain	AA	WN	RWF (ours)
Regular	28.82%	38.63%	46.34%	4.14%
Curriculum	62.37%	61.58%	33.41%	2.31%
Causal	4.61%	2.91%	28.48%	1.67%

Table 10: *Advection*: Relative L^2 errors of training PINNs with different weight parameterizations and training strategies.

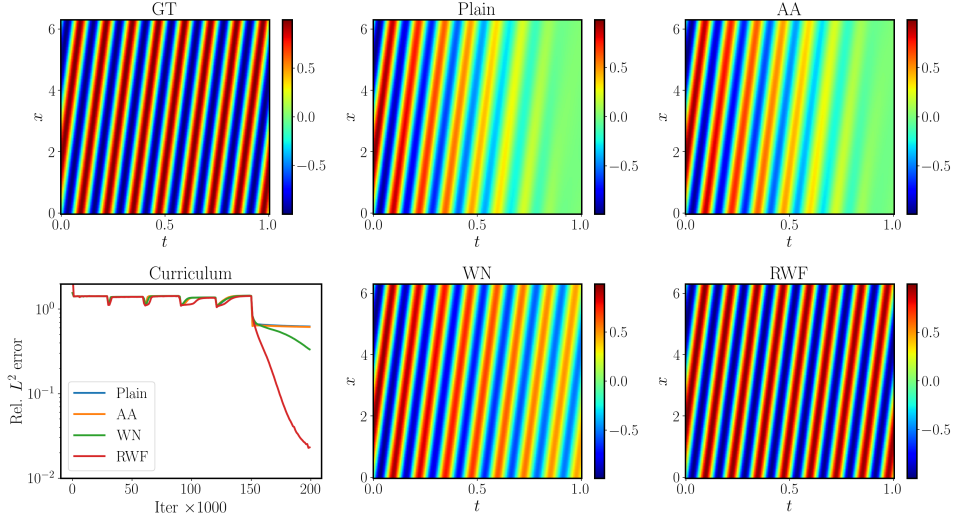


Figure 16: *Adition*: Predicted solutions of training PINNs with different weight parameterizations using curriculum training, as well as the evolution of the associated relative L^2 errors during training.

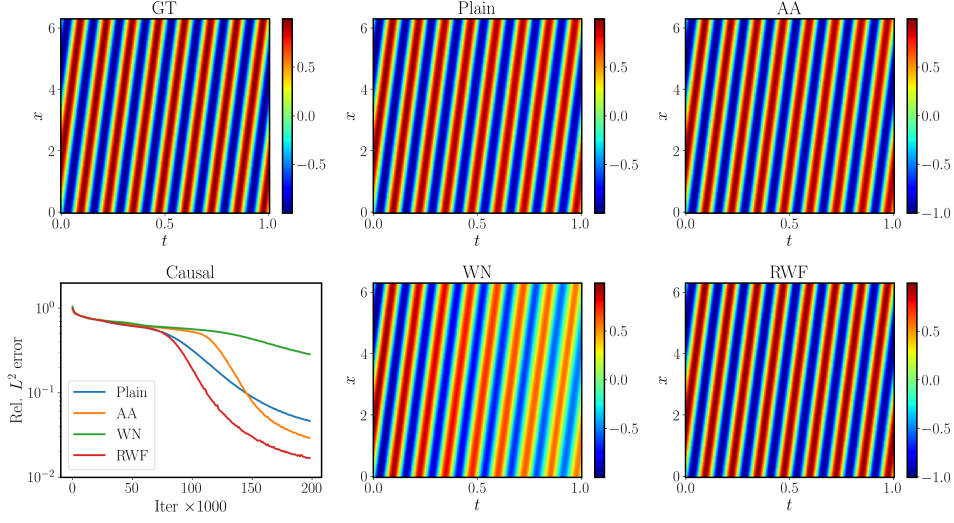


Figure 17: *Adition*: Predicted solutions of training PINNs with different weight parameterizations using causal training, as well as the evolution of the associated relative L^2 errors during training.

K.2 NAVIER-STOKES EQUATION

The underlying PDE system for this benchmark takes the form

$$\mathbf{u} \cdot \nabla \mathbf{u} + \nabla p - \frac{1}{Re} \Delta \mathbf{u} = 0, \quad (x, y) \in (0, 1)^2, \quad (\text{K.9})$$

$$\nabla \cdot \mathbf{u} = 0, \quad (x, y) \in (0, 1)^2, \quad (\text{K.10})$$

$$\mathbf{u} = (1, 0), \quad (x, y) \text{ on } \Gamma_1, \quad (\text{K.11})$$

$$\mathbf{u} = (0, 0), \quad (x, y) \text{ on } \Gamma_2. \quad (\text{K.12})$$

Here Γ_1 is the top boundary of a square cavity, while Γ_2 denotes the other three sides of the cavity. We represent the unknown solution u, v, p using a neural network \mathbf{u}_θ :

$$[x, y] \xrightarrow{\mathbf{u}_\theta} [u_\theta, v_\theta, p_\theta]. \quad (\text{K.13})$$

Then, the PDE residuals are defined by

$$\mathcal{R}_\theta^u = u_\theta \frac{\partial u_\theta}{\partial x} + v_\theta \frac{\partial u_\theta}{\partial y} + \frac{\partial p_\theta}{\partial x} - \frac{1}{\text{Re}} \left(\frac{\partial^2 u_\theta}{\partial x^2} + \frac{\partial^2 u_\theta}{\partial y^2} \right), \quad (\text{K.14})$$

$$\mathcal{R}_\theta^v = u_\theta \frac{\partial v_\theta}{\partial x} + u_\theta \frac{\partial v_\theta}{\partial y} + \frac{\partial p_\theta}{\partial y} - \frac{1}{\text{Re}} \left(\frac{\partial^2 u_\theta}{\partial x^2} + \frac{\partial^2 u_\theta}{\partial y^2} \right), \quad (\text{K.15})$$

$$\mathcal{R}_\theta^c = \frac{\partial u_\theta}{\partial x} + \frac{\partial v_\theta}{\partial y}. \quad (\text{K.16})$$

Given these residuals, along with a set of appropriate boundary conditions, we can now formulate a loss function for training a physics-informed neural network as

$$\mathcal{L}(\theta) = \lambda_u \mathcal{L}_u(\theta) + \lambda_v \mathcal{L}_v(\theta) + \lambda_{r_u} \mathcal{L}_{r_u}(\theta) + \lambda_{r_v} \mathcal{L}_{r_v}(\theta) + \lambda_{r_c} \mathcal{L}_{r_c}(\theta), \quad (\text{K.17})$$

with

$$\mathcal{L}_{u_b}(\theta) = \frac{1}{N_b} \sum_{i=1}^{N_b} [u(x_b^i, y_b^i) - u_b^i]^2, \quad (\text{K.18})$$

$$\mathcal{L}_{v_b}(\theta) = \frac{1}{N_b} \sum_{i=1}^{N_b} [v(x_b^i, y_b^i) - v_b^i]^2, \quad (\text{K.19})$$

$$\mathcal{L}_{r_u}(\theta) = \frac{1}{N_r} \sum_{i=1}^{N_r} [R_\theta^u(x_r^i, y_r^i)]^2, \quad (\text{K.20})$$

$$\mathcal{L}_{r_v}(\theta) = \frac{1}{N_r} \sum_{i=1}^{N_r} [R_\theta^v(x_r^i, y_r^i)]^2, \quad (\text{K.21})$$

$$\mathcal{L}_{r_c}(\theta) = \frac{1}{N_r} \sum_{i=1}^{N_r} [R_\theta^c(x_r^i, y_r^i)]^2, \quad (\text{K.22})$$

where $\{(x_b^i, y_b^i), u_b^i\}_{i=1}^{N_b}$ and $\{(x_b^i, y_b^i), v_b^i\}_{i=1}^{N_b}$ denote the boundary data for the two velocity components at the domain boundaries Γ_1 and Γ_2 , respectively, while $\{(x_r^i, y_r^i)\}_{i=1}^{N_r}$ is a set of collocation points for enforcing the PDE constraints. All of them are sampled randomly at each iteration of gradient descent. In experiments, we set $N_b = 256$, $N_r = 1024$ and $\lambda_u = \lambda_v = 100$, $\lambda_{r_u} = \lambda_{r_v} = \lambda_{r_c} = 1$.

We employ an MLP (5 layers, 128 channels, tanh activations) to represent the latent variables of interest, and train the network with different parameterizations for 10^5 iterations using the Adam optimizer (Kingma & Ba, 2014) with a start learning rate of 10^{-3} and an exponential decay by a factor of 0.9 for every 2,000 training iterations. Moreover, we use a modified MLP architecture (see definition below) and curriculum training to enhance the model stability and performance. For the curriculum training, we minimize the loss with $Re = 100$ and $Re = 500$ for 2×10^4 iterations sequentially and change the Reynolds number to $Re = 1,000$ for the rest of the training. The resulting relative L^2 errors are reported in Table 11. We can see that RWF performs the best among all parameterizations by a large margin. Some visualizations are shown in Figure 4 and Figure 18. We attribute this significant performance improvements to the fact that PINN models often suffer from poor initializations, and RWF precisely mitigates this by being able to reach better local minima that are located further away from the model initialization neighborhood.

Navier-Stokes	Plain	AA	WN	RWF (ours)
MLP	39.25%	34.09%	30.98%	6.67%
Modified MLP	3.51%	3.87%	3.75%	2.46%

Table 11: *Navier-Stokes*: Relative L^2 errors of training conventional MLPs and modified MLPs with different weight parameterizations, respectively.

Modified MLP: In (Wang et al., 2021b) Wang *et al.* proposed a novel architecture that was demonstrated to outperform conventional MLPs across a variety of PINNs benchmarks. Here, we will refer to this architecture as "modified MLP". The forward pass of a L -layer modified MLP is defined as follows

$$U = \sigma(W_1 x + b_1), \quad V = \sigma(W_2 x + b_2), \quad (K.23)$$

$$H^{(1)} = \sigma(W^{(1)} x + b^{(1)}), \quad (K.24)$$

$$Z^{(l)} = \sigma(W^{(l+1)} H^{(k)} + b^{(l+1)}), \quad l = 1, \dots, L-1, \quad (K.25)$$

$$H^{(l+1)} = (1 - Z^{(l)}) \odot U + Z^{(l)} \odot V, \quad l = 1, \dots, L-1, \quad (K.26)$$

$$u_\theta(x) = W^{(L+1)} H^{(L)} + b^{(L+1)}, \quad (K.27)$$

where σ denotes a nonlinear activation function, \odot denotes a point-wise multiplication. All trainable parameters are given by

$$\theta = \{W_1, b_1, W_2, b_2, (W^{(l)}, b^{(l)})_{l=1}^{L+1}\}. \quad (K.28)$$

This architecture is almost the same as a standard MLP network, with the addition of two encoders and a minor modification in the forward pass. Specifically, the inputs x are embedded into a feature space via two encoders U, V , respectively, and merged in each hidden layer of a standard MLP using a point-wise multiplication.

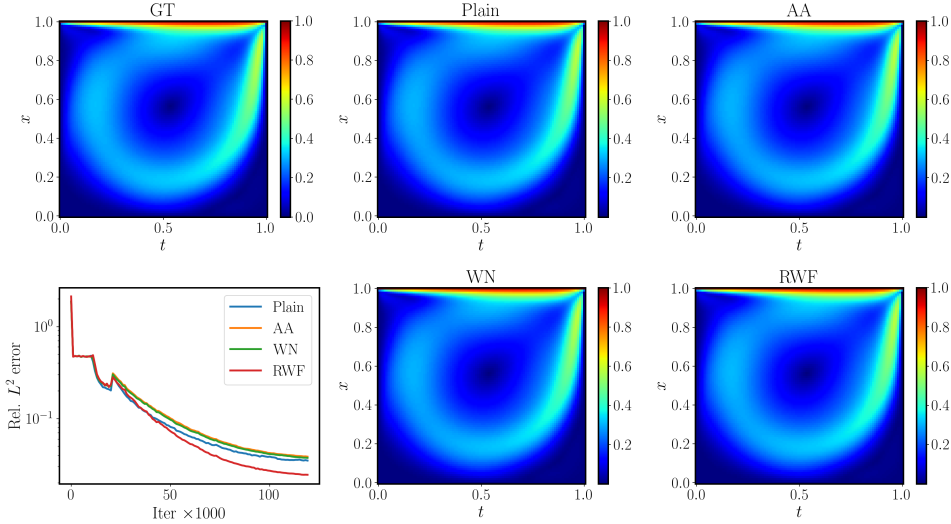


Figure 18: *Naiver-Stokes*: Predicted solutions obtained by modified MLPs with different weight parameterization, as well as the evolution of the associated relative L^2 errors during training.

L LEARNING OPERATORS

Overview of DeepONets: DeepONet is supposed to approximate an operator G between functional spaces. DeepONet consists of two separate neural networks referred to as the "branch net" and "trunk net", respectively. The branch net takes a vector a as input and returns a features embedding $[b_1, b_2, \dots, b_q]^T \in \mathbb{R}^q$ as output, where $a = [a(x_1), a(x_2), \dots, a(x_m)]$ represents a function a evaluated at a collection of fixed locations $\{x_i\}_{i=1}^m$. The trunk net takes the continuous coordinates y as inputs, and outputs a features embedding $[t_1, t_2, \dots, t_q]^T \in \mathbb{R}^q$. The DeepONet output is obtained by merging the outputs of the branch and trunk networks together via a dot product

$$G_\theta(a)(y) = \sum_{k=1}^q \underbrace{b_k(a(x_1), a(x_2), \dots, a(x_m))}_{\text{branch}} \underbrace{t_k(y)}_{\text{trunk}}, \quad (L.1)$$

where θ denotes the collection of all trainable weight and bias parameters in the branch and trunk networks. These parameters can be optimized by minimizing the following mean square error loss

$$\mathcal{L}(\theta) = \frac{1}{NP} \sum_{i=1}^N \sum_{j=1}^P \left| G_{\theta}(\mathbf{a}^{(i)})(\mathbf{y}_j^{(i)}) - G(\mathbf{a}^{(i)})(\mathbf{y}_j^{(i)}) \right|^2 \quad (\text{L.2})$$

$$= \frac{1}{NP} \sum_{i=1}^N \sum_{j=1}^P \left| \sum_{k=1}^q b_k(\mathbf{a}^{(i)}(\mathbf{x}_1), \dots, \mathbf{a}^{(i)}(\mathbf{x}_m)) t_k(\mathbf{y}_j^{(i)}) - G(\mathbf{a}^{(i)})(\mathbf{y}_j^{(i)}) \right|^2, \quad (\text{L.3})$$

where $\{\mathbf{a}^{(i)}\}_{i=1}^N$ denotes N separate input functions sampled from a function space \mathcal{U} . For each $\mathbf{a}^{(i)}$, $\{\mathbf{y}_j^{(i)}\}_{j=1}^P$ are P locations in the domain of $G(\mathbf{a}^{(i)})$, and $G(\mathbf{a}^{(i)})(\mathbf{y}_j^{(i)})$ is the corresponding output data evaluated at $\mathbf{y}_j^{(i)}$. Contrary to the fixed sensor locations of $\{\mathbf{x}_i\}_{i=1}^m$, we remark that the locations of $\{\mathbf{y}_j^{(i)}\}_{j=1}^P$ may vary for different i , thus allowing us to construct a continuous representation of the output function $G(a)$.

Remark: All parameterizations (AA, WN, RWF) are applied to every dense layer of the DeepONet architecture (in the cases where such parametrizations are employed).

Case	Plain	AA	WN	RWF
DR	$1.09\% \pm 0.53\%$	$0.95\% \pm 0.46\%$	$0.97\% \pm 0.46\%$	$0.50\% \pm 0.26\%$
Darcy	$2.03\% \pm 1.54\%$	$2.06\% \pm 1.70\%$	$2.05\% \pm 2.00\%$	$1.67\% \pm 1.70\%$
Burgers	$5.11\% \pm 3.79\%$	$4.71\% \pm 3.39\%$	$4.37\% \pm 2.63\%$	$2.46\% \pm 2.05\%$

Table 12: *Learning operators*: Relative L^2 errors of trained (physics-informed) DeepONets over the test data-set of different examples.

L.1 DIFFUSION-REACTION

The underlying PDE for this benchmark takes the form

$$\frac{\partial u}{\partial t} = D \frac{\partial^2 u}{\partial x^2} + ku^2 + a(x), \quad (x, t) \in (0, 1) \times (0, 1], \quad (\text{L.4})$$

subject to zero initial and boundary conditions.

Data Generation: We sample $N = 5,000$ input functions $a(x)$ from a GRF with length scale $l = 0.2$ and solve the diffusion-reaction system using a second-order implicit finite difference method on a 100×100 equispaced grid. To generate the training data, we randomly take $P = 100$ measurements from each solution. The test data-set contains another 100 solutions evaluated at the same mesh.

We represent the solution operator by a DeepONet G_{θ} , where the branch and trunk networks are two separate MLPs (5 layers, 64 channels, tanh activations). The model is trained for 5×10^4 iterations using the Adam optimizer (Kingma & Ba, 2014) with a start learning rate of 10^{-3} and an exponential decay by a factor of 0.9 for every 1000 steps. The mean and standard deviation of the relative L^2 errors over the test data-set are shown in Table 12. Figure 19 provides several representative predictions using RWF.

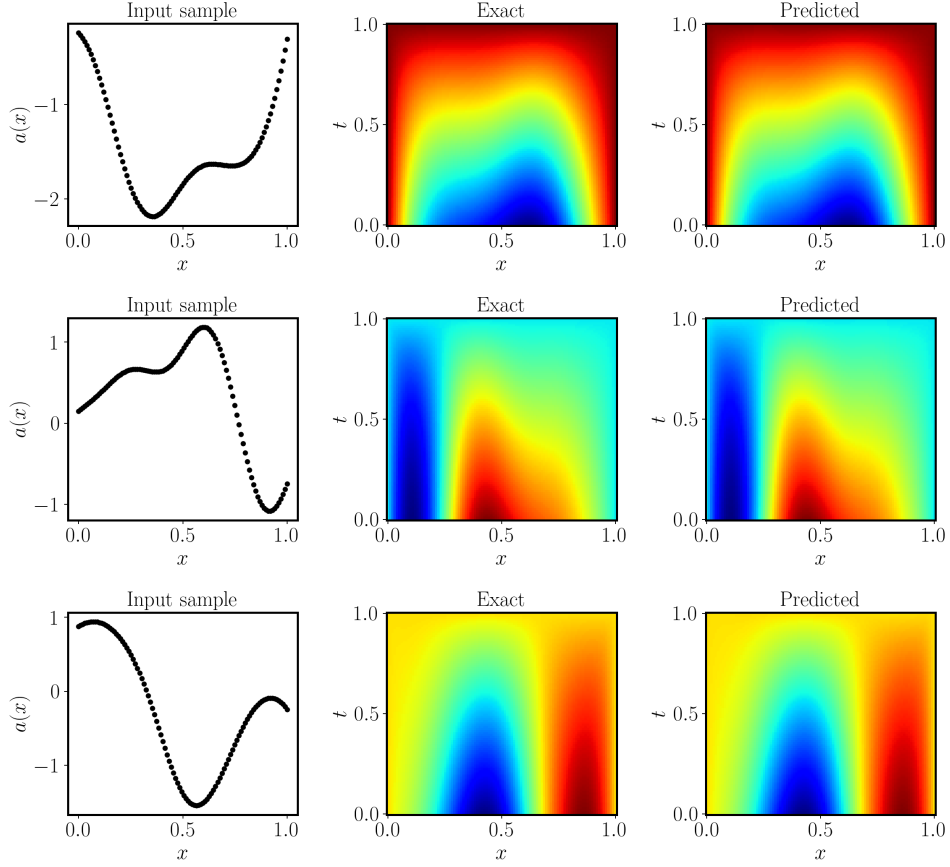


Figure 19: *Diffusion-reaction (DR) PDE*: Predicted solutions of a trained DeepONet with random weight factorization, corresponding to randomly chosen input samples in the test data-set.

L.2 Darcy Flow

The PDE system for this benchmark takes the form

$$-\nabla \cdot (a \cdot \nabla u) = 1, \quad (x, y) \in (0, 1)^2, \quad (\text{L.5})$$

$$u = 0, \quad (x, y) \in \partial(0, 1)^2. \quad (\text{L.6})$$

Data Generation: We sample the coefficient function a from a Gaussian random field with a length scale $l = -0.5$ and solve the associated Darcy flow using finite element method. The training data contains 2,000 solutions evaluated at a 64×64 uniform mesh while the test data contains 100 solutions on the same mesh.

We represent the solution operator by a DeepONet G_θ , where the branch network is a convolutional neural network (CNN) for extracting latent feature representation of the input coefficients and the trunk network is a 4-layer MLP with GELU activations and 128 neurons per hidden layer. We train each model with different parameterizations for 5×10^4 iterations using the Adam optimizer (Kingma & Ba, 2014) with a start learning rate of 10^{-3} and an exponential decay by a factor of 0.9 for every 1000 steps. The results are summarized in Table 12 and some predicted solutions are plotted in Figure 20.

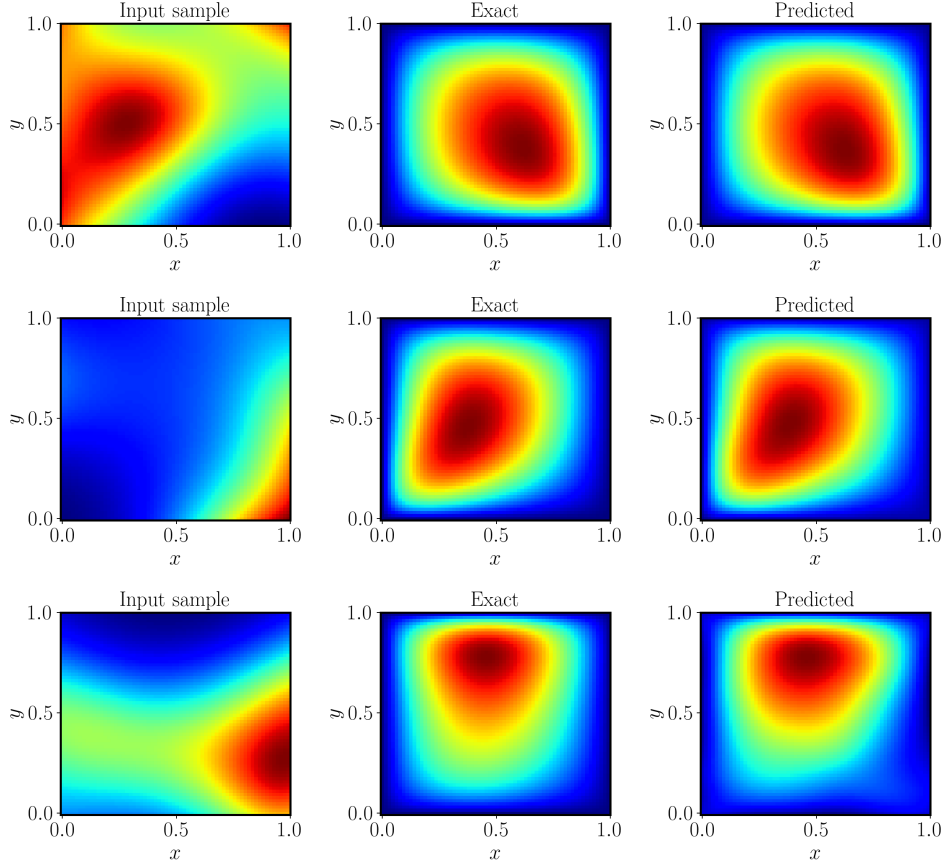


Figure 20: *Darcy PDE*: Predicted solutions of a trained DeepONet with random weight factorization, corresponding to randomly chosen input samples in the test data-set.

L.3 BURGERS' EQUATION

Recall the one-dimensional Burgers' equation is given by

$$\frac{du}{dt} + u \frac{du}{dx} - \nu \frac{d^2u}{dx^2} = 0, \quad (x, t) \in (0, 1) \times (0, 1], \quad (\text{L.7})$$

subject to initial and the periodic boundary conditions

$$u(x, 0) = a(x), \quad x \in (0, 1), \quad (\text{L.8})$$

Data Generation: The training data only consists of 1,000 input functions a sampled from a Gaussian random field $\sim \mathcal{N}(0, 25^2(-\Delta + 5^2I)^{-4})$. To generate the test data-set, we sample another 100 input functions from the same Gaussian random field and solve the Burgers' equation using the Chebfun package Driscoll et al. (2014) with a spectral Fourier discretization and a fourth-order stiff time-stepping scheme (ETDRK4) Cox & Matthews (2002) with a time-step size of 10^{-4} . Temporal snapshots of the solution are saved every $\Delta t = 0.01$ to give us 101 snapshots in total. Consequently, the test data-set contains 500 realizations evaluated at a 100×101 spatio-temporal grid.

Our objective here is to learn the solution operator mapping initial conditions $a(x)$ to the associated full spatio-temporal solution $u(x, t)$. Here proceed by representing the solution operator by a modified DeepONet architecture Wang et al. (2021d) outlined below. To impose the periodic the exact boundary condition, we apply a Fourier feature mapping to the input coordinates before passing them through the trunk network

$$[x, t] \rightarrow [\cos(2\pi x), \sin(2\pi x), t]. \quad (\text{L.9})$$

Then the PDE residual is then defined by

$$R_{\theta}[a] = \frac{\partial G_{\theta}(\mathbf{a})}{\partial t} + G_{\theta}(\mathbf{a}) \frac{\partial G_{\theta}(\mathbf{a})}{\partial x} - \nu \frac{\partial^2 G_{\theta}(\mathbf{a})}{\partial x^2}, \quad (\text{L.10})$$

Consequently, a physics-informed DeepONet can be trained by minimizing the following weighted loss function

$$\mathcal{L}(\theta) = \lambda_{ic} \mathcal{L}_{ic}(\theta) + \lambda_r \mathcal{L}_r(\theta), \quad (\text{L.11})$$

where

$$\mathcal{L}_{ic}(\theta) = \frac{1}{NP} \sum_{i=1}^N \sum_{j=1}^P \left| G_{\theta}(\mathbf{a}^{(i)})(x_{ic,j}^{(i)}, 0) - u^{(i)}(x_{ic,j}^{(i)}) \right|^2, \quad (\text{L.12})$$

$$\mathcal{L}_r(\theta) = \frac{1}{NQ} \sum_{i=1}^N \sum_{j=1}^Q \left| R_{\theta}^{(i)}(x_{r,j}^{(i)}, t_{r,j}^{(i)}) \right|^2. \quad (\text{L.13})$$

For this example, we take $N = 64$, $P = 100$ and $Q = 512$, which means that we randomly sample $N = 64$ input functions from the training data-set and $Q = 512$ collocation points inside the computational domain. In particular, we set $\lambda_{ic} = 100$, $\lambda_r = 1$ for better enforcing the initial condition across different input samples. The model with different parameterizations is trained for 10^5 iterations using the Adam optimizer (Kingma & Ba, 2014) with a start learning rate of 10^{-3} and an exponential decay by a factor of 0.9 for every 2,000 steps. We report the test errors in Table 12 and visualize some predicted solutions in Figure 21.

Modified DeepONet: Wang et al. (2021d) modify the forward pass of an L-layer DeepONet as follows

$$\mathbf{U} = \phi(\mathbf{W}_a \mathbf{a} + \mathbf{b}_a), \quad \mathbf{V} = \phi(\mathbf{W}_y \mathbf{y} + \mathbf{b}_y), \quad (\text{L.14})$$

$$\mathbf{H}_a^{(1)} = \phi(\mathbf{W}_a^{(1)} \mathbf{a} + \mathbf{b}_a^{(1)}), \quad \mathbf{H}_y^{(1)} = \phi(\mathbf{W}_y^{(1)} \mathbf{y} + \mathbf{b}_y^{(1)}), \quad (\text{L.15})$$

$$\mathbf{Z}_a^{(l)} = \phi(\mathbf{W}_a^{(l)} \mathbf{H}_a^{(l)} + \mathbf{b}_a^{(l)}), \quad \mathbf{Z}_y^{(l)} = \phi(\mathbf{W}_y^{(l)} \mathbf{H}_y^{(l)} + \mathbf{b}_y^{(l)}), \quad l = 1, 2, \dots, L-1, \quad (\text{L.16})$$

$$\mathbf{H}_a^{(l+1)} = (1 - \mathbf{Z}_a^{(l)}) \odot \mathbf{U} + \mathbf{Z}_a^{(l)} \odot \mathbf{V}, \quad l = 1, \dots, L-1, \quad (\text{L.17})$$

$$\mathbf{H}_y^{(l+1)} = (1 - \mathbf{Z}_y^{(l)}) \odot \mathbf{U} + \mathbf{Z}_y^{(l)} \odot \mathbf{V}, \quad l = 1, \dots, L-1, \quad (\text{L.18})$$

$$\mathbf{H}_a^{(L)} = \phi(\mathbf{W}_a^{(L)} \mathbf{H}_a^{(L-1)} + \mathbf{b}_a^{(L)}), \quad \mathbf{H}_y^{(L)} = \phi(\mathbf{W}_y^{(L)} \mathbf{H}_y^{(L-1)} + \mathbf{b}_y^{(L)}), \quad (\text{L.19})$$

$$G_{\theta}(\mathbf{a})(\mathbf{y}) = \left\langle \mathbf{H}_a^{(L)}, \mathbf{H}_y^{(L)} \right\rangle, \quad (\text{L.20})$$

where \odot denotes point-wise multiplication, ϕ denotes a activation function, and θ represents all trainable parameters of the DeepONet model. In particular, $\{\mathbf{W}_a^{(l)}, \mathbf{b}_a^{(l+1)}\}_{l=1}^{L+1}$ and $\{\mathbf{W}_y^{(l)}, \mathbf{b}_y^{(l+1)}\}_{l=1}^{L+1}$ are the weights and biases of the branch and trunk networks, respectively. we embed the DeepONet inputs \mathbf{a} and \mathbf{y} into a high-dimensional feature space via two encoders \mathbf{U}, \mathbf{V} , respectively. Instead of just merging the propagated information in the output layer of the branch and trunk networks, we merge the embeddings \mathbf{U}, \mathbf{V} in each hidden layer of these two sub-networks using a point-wise multiplication (equation (L.17) - (L.18)). Heuristically, this design may not only help input signals propagate through the DeepONet, but also enhance its capability of representing non-linearity due to the extensive use of point-wise multiplications.

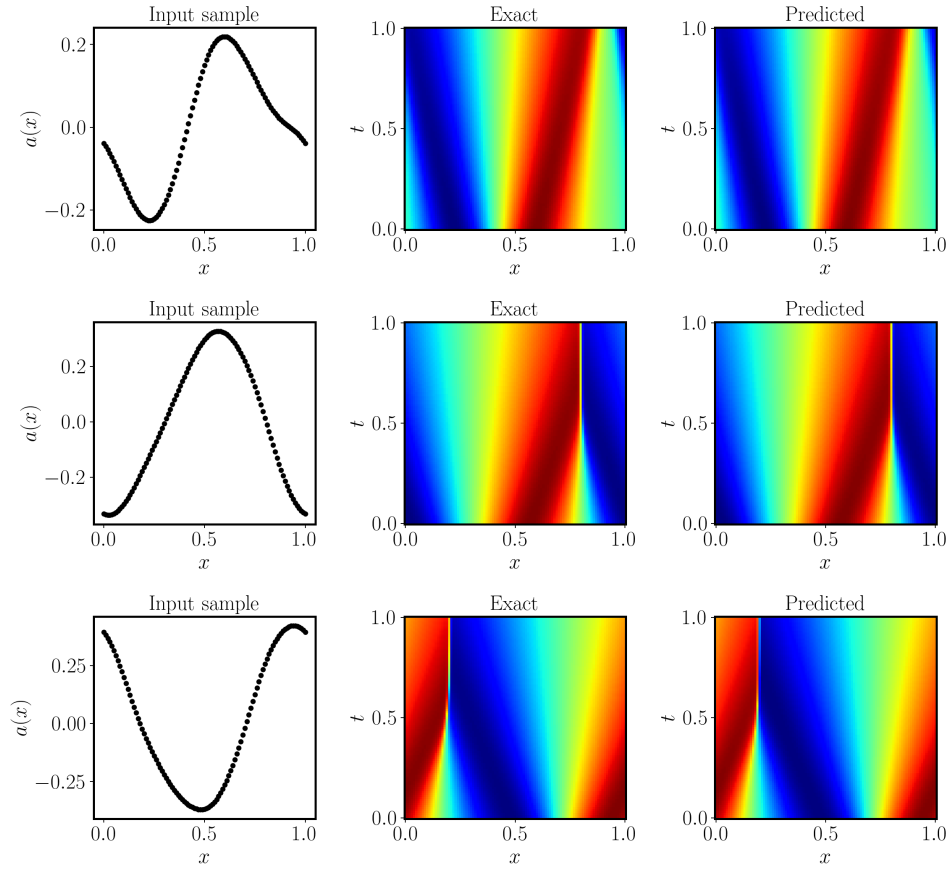


Figure 21: *Burgers PDE*: Predicted solutions of a trained physics-informed DeepONet with random weight factorization, corresponding to randomly chosen input samples in the test data-set.